Determination of atomic multiphoton-ionization phases by trichromatic multichannel wave-packet interferometry

K. Eickhoff ●, D. Köhnke ●, L. Feld, T. Bayer, and M. Wollenhaupt ●*

Carl von Ossietzky Universität Oldenburg, Institut für Physik, Carl-von-Ossietzky-Straße 9-11, D-26129 Oldenburg, Germany

We present the unambiguous determination of quantum phases in the multiphoton ionization (MPI) of potassium atoms by using a multichannel photoelectron interferometry scheme based on trichromatic pulse shaping. The colors of the laser field are chosen to produce three energetically separated photoelectron interferograms in the continuum. While the red pulse is two-photon resonant with the $3d$ state resulting in a $(2 + 1)$ resonance-enhanced MPI (REMPI), a $(1 + 2)$ REMPI occurs via the nonresonant intermediate $4p$ state with an initial green or blue pulse. We show that ionization via a nonresonant intermediate state lifts the degeneracy of photoelectron interferograms from pathways consisting of permutations of the colors. The analysis of the interferograms reveals a phase shift of $\pm\pi/2$ depending on the sign of the detunings in the $(1 + 2)$ REMPI pathways. In addition, we demonstrate that the photoionization time delay in the resonant $(2 + 1)$ REMPI pathway gives rise to a linear spectral phase in the photoelectron spectra. Insights into the underlying MPI processes are gained through an analytic perturbative description and numerical simulations of a trichromatic driven three-level system coupled to the continuum.

I. INTRODUCTION

Being at the heart of atomic, molecular, and optical physics, photoionization has been studied for over a century, both experimentally and theoretically. Initially, Einstein gave a theoretical interpretation of the photoelectric effect in his seminal 1905 publication [1], where he envisioned the possibility of processes in which an "energy quantum of emitted light can obtain its energy from multiple incident energy quanta." Subsequently, a quantum-mechanical description of two-photon transitions was given by Göppert-Mayer in 1931 [2] paving the way to our modern understanding of multiphoton ionization (MPI). Sophisticated MPI schemes combined with highly differential detection techniques for the time-, energy-, and angle-resolved measurements have established the field of nonlinear photoelectron spectroscopy yielding numerous applications in fundamental and applied physics, as described in monographs [3–11] and review articles [12–16]. Attosecond electron dynamics [17,18], coherent control of atomic and molecular dynamics by shaped laser pulses [19–24], and the generation of free electron vortices [25–29] are examples for the wide variety of modern topics in atomic and molecular MPI. In addition to measure the photoelectron probability density distribution the use of interferometric techniques [30] has made it possible to determine the phase of photoelectron wave packets. Quantum-mechanical phases are key to coherent control [31–35] and essential for the complete characterization of the wave function [36–38]. Knowledge about the phase of photoelectron wave functions from atomic [39–41] and molecular [42–44] photoionization processes provides insights into the underlying dynamics [45] accompanied with photoemission phases

and time delays [46–52]. In those measurements, the superposition of multiple partial waves gave rise to phase-sensitive interference patterns that allowed the quantum-mechanical phase to be reconstructed. In general, the exact shape of an interferogram is determined by the ionizing radiation's optical phase and the additional quantum phase due to the ionization dynamics. To distinguish between these two phases, in the following, the phase introduced by laser radiation will be referred to as the *optical phase*, while the quantum-mechanical phase resulting from ionization dynamics will be referred to as the *MPI phase*. Very recently, building on the results presented in [40], MPI phases from multiple intermediate states were investigated in the photoionization of helium atoms [41].

In this paper, we demonstrate a trichromatic MPI scheme to decouple the MPI phase measurement from the optical phase control for an unambiguous determination of the MPI phase. We exemplify our scheme on the trichromatic three-photon ionization of potassium atoms to investigate the MPI phases due to the intermediate resonances. It has been shown that interference patterns in photoelectron spectra from multichromatic MPI, such as bichromatic photoelectron vortices, are sensitive to the carrier-envelope phase (CEP) [28]. However, we have recently demonstrated a pulse-shaper-based trichromatic MPI scheme for quantum state holography [53] in which the photoelectron hologram is sensitive to the MPI phases and the relative optical phases between the colors in the trichromatic pulse sequence but insensitive to the CEP. While in the proof-of-principle experiment in [53] the focus is on optical phase control of *one single* photoelectron hologram and the imprinted time-evolution phases, here we apply and extend the technique by simultaneously using *multiple* photoelectron interferences to detect acquired MPI phases along different quantum pathways. To this end, we use temporally overlapping trichromatic fields with the central frequencies of

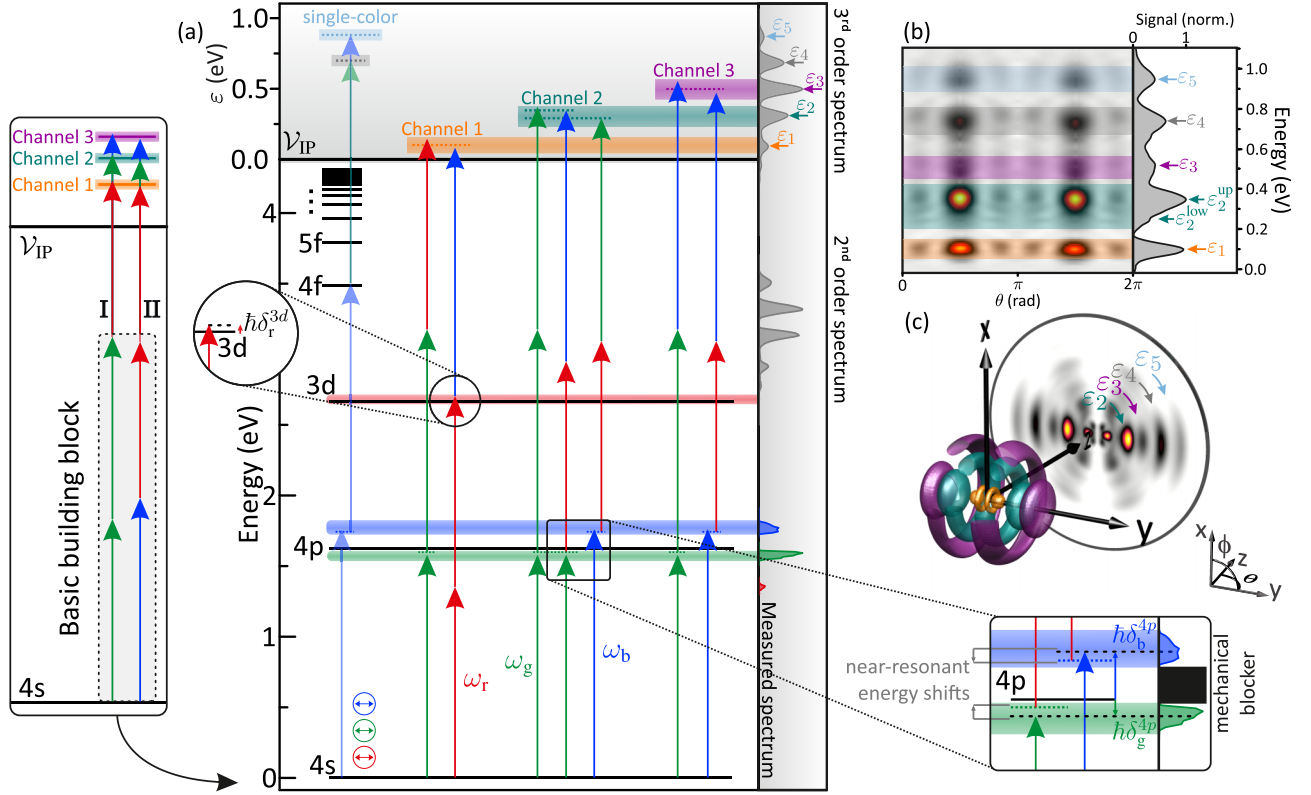*Corresponding author: Matthias.Wollenhaupt@uol.de

FIG. 1. (a) Excitation scheme of potassium atoms interacting perturbatively with a linearly polarized trichromatic field for multichannel interferometry together with the experimental multiphoton spectrum. We use temporally overlapping trichromatic pulses with frequencies $2\omega_g = \omega_r + \omega_b$ (black dashed box in the left figure) to achieve interference of photoelectrons by MPI with different combinations of red, green, and blue photons. The interference leads to three energetically separated photoelectron interferograms in the interference channels 1–3 (highlighted in orange, petrol blue, and violet). The frequencies are spectrally confined to be either two-photon resonant with the $3d$ state, i.e., $2\omega_r \simeq \omega_{3d}$, or one-photon near but nonresonant with the $4p$ state, i.e., $\omega_g \lesssim \omega_{4p} < \omega_b$ (right bottom inset). The near-resonant excitation of the $4p$ state lifts the degeneracy of the frequency mixing pathways and causes the second channel to split into two bands (ε_2^{low} and ε_2^{up}) around ε_2. (b) Measured and Abel-inverted photoelectron signals in polar coordinates. (c) Measured and tomographically reconstructed 3D PMD with color-coded interference channels at ε_1-ε_3.

the red (ω_r), green (ω_g), and blue (ω_b) spectral bands chosen such that $2\omega_g = \omega_r + \omega_b$. Due to this frequency condition, the laser pulses create free electron wave packets forming interferograms in three different photoelectron kinetic-energy windows, referred to as interference channels. By design, the interferograms consist of wave packets from $(1+2)$ resonance enhanced MPI (REMPI) via the $4p$ state or $(2+1)$ REMPI via the $3d$ state. The observed interference patterns are sensitive to the MPI phases as well as the relative optical phases. Motivated by the concerted generation of multiple interferograms in one photoelectron spectrum, the technique is termed *trichromatic multichannel wave-packet interferometry*. Due to the temporal overlap of the fields, the observed interferograms also map the phases introduced by transiently populated atomic bound states. The MPI phases are extracted from energy-resolved photoelectron spectra measured as a function of the relative optical phase of the green spectral component. In the resulting phase-resolved measurements, the quantum phases manifest as relative phase shifts between the interferograms in the different channels. The interpretation of the experimental results is supported by the analysis of a model system consisting of a three-level atom coupled to the continuum. To simulate laser-induced bound and ionization

dynamics we study both the analytic perturbative description and the numeric solution of the time-dependent Schrödinger equation (TDSE).

II. PHYSICAL SYSTEM AND THEORY

In this section, we present the physical system studied by our shaper-based multichannel interferometry scheme. We provide a theoretical description of the measured photoelectron momentum distributions (PMDs) with emphasis on their dependence on the optical and MPI phases. Based on the theoretical model, we analyze our experimental results in Sec. IV.

A. Physical system

The excitation scheme of potassium atoms interacting perturbatively with parallel linearly polarized (PLP) trichromatic fields is shown in Fig. 1(a). In the experiment, we use temporally overlapping trichromatic pulses to produce the interference of multiple MPI pathways from *different* combinations of red (r), green (g), and blue (b) photons, i.e., single-color and frequency mixing contributions [54] in the photoelectron spectrum. Usually, in multichromatic MPI, only

TABLE I. Interference channels with the relevant resonance-enhanced pathways together with the theoretical MPI phases and the corresponding MPI phase differences. In all cases we use $\delta_2 \geqslant 0$ according to the experiment.

Channel	Name	Path	Theoretical MPI phase χ	Theoretical MPI phase difference γ
1	$\mathcal{R}_{\mathrm{I}}$	ggr	$\chi^{\mathrm{non}}_{\delta_1<0} = \frac{3\pi}{2}$	$\gamma^{(1)}_{\mathrm{theo}}(\varepsilon) = \frac{\pi}{2} - \xi(\varepsilon)$
	$\mathcal{R}_{\mathrm{II}}$	rrb	$\chi^{\mathrm{res}}_{\delta_1<0}(\varepsilon) = \pi + \xi(\varepsilon)$	
2	$\mathcal{G}_{\mathrm{I}}$	ggg	$\chi^{\mathrm{non}}_{\delta_1<0} = \frac{3\pi}{2}$	$\gamma^{(2,\mathrm{low})}_{\mathrm{theo}} = \pi$
	$\mathcal{G}^{\mathrm{low}}_{\mathrm{II}}$	brg	$\chi^{\mathrm{non}}_{\delta_1>0} = \frac{\pi}{2}$	
	$\mathcal{G}_{\mathrm{I}}$	ggg	$\chi^{\mathrm{non}}_{\delta_1<0} = \frac{3\pi}{2}$	$\gamma^{(2,\mathrm{up})}_{\mathrm{theo}} = 0$
	$\mathcal{G}^{\mathrm{up}}_{\mathrm{II}}$	grb	$\chi^{\mathrm{non}}_{\delta_1<0} = \frac{3\pi}{2}$	
3	$\mathcal{B}_{\mathrm{I}}$	ggb	$\chi^{\mathrm{non}}_{\delta_1<0} = \frac{3\pi}{2}$	$\gamma^{(3)}_{\mathrm{theo}} = \pi$
	$\mathcal{B}_{\mathrm{II}}$	brb	$\chi^{\mathrm{non}}_{\delta_1>0} = \frac{\pi}{2}$	

permutations of a given color combination connect the same initial and final states. However, by appropriate choice of the field's frequencies, even different color combinations give rise to interference in several energetically separated final states. In the experiment, the photon energies are chosen to ensure the same number of photons (*three*) not only in each frequency mixing pathway but also in the green single-color pathway. Consequently, the photoelectron interferograms are insensitive to CEP variations, but are controlled by the relative optical phases. To maximize the generation of the frequency mixing signals, all three colors overlap in time. The interference of frequency mixing pathways consisting of different photon combinations is observed when the central frequencies and the time delays of the trichromatic field are chosen such that

$$2\omega_{\mathrm{g}} = \omega_{\mathrm{r}} + \omega_{\mathrm{b}} < \omega_{\mathrm{IP}}, \qquad (1)$$

$$\tau_{\mathrm{r}} = \tau_{\mathrm{g}} = \tau_{\mathrm{b}}, \qquad (2)$$

where ω_{r}, ω_{g}, ω_{b} and τ_{r}, τ_{g}, τ_{b} denote the central frequencies and time delays of the red (r), green (g), and blue (b) spectral components. $\mathcal{V}_{\mathrm{IP}} = \hbar\omega_{\mathrm{IP}}$ describes the ionization potential. The spectral and temporal conditions (1) and (2) form the basic building block of the presented scheme which is visualized by the dashed box in the left inset of Fig. 1(a). When both conditions are met, the trichromatic field simultaneously generates three energetically separated photoelectron interferograms in the continuum. In the following, the corresponding energy windows centered around ε_1, ε_2, and ε_3 will be referred to as *interference channels* [see Fig. 1(a)]. To study the MPI phases induced by intermediate resonant states, the frequencies are further chosen to be either two-photon resonant with the 3*d* state, i.e., $2\omega_{\mathrm{r}} = \omega_{3d}$, or one-photon near resonant with the 4*p* state, i.e., $\omega_{\mathrm{g}} \lesssim \omega_{4p} < \omega_{\mathrm{b}}$. Since the (near-)resonant excitation is more efficient, the 4*p* and 3*d* intermediate states select the resonance-enhanced pathways, listed in Table I.

For example, the interferogram in channel 1 is created by the interference of photoelectrons via the resonance-enhanced MPI pathways $\mathcal{R}_{\mathrm{I}}$ and $\mathcal{R}_{\mathrm{II}}$. The pathway $\mathcal{R}_{\mathrm{I}}$, denoted as (ggr), describes the absorption of two green (gg) photons and one red (r) photon in this order. Similarly, the pathway $\mathcal{R}_{\mathrm{II}}$, denoted as (rrb), describes the absorption of two red (rr) photons and one blue (b) photon. The other resonance-enhanced pathways leading to the channels 2 and

3 are labeled in the same way. Even though the color combinations of the individual MPI pathways are quite different, the total optical phase difference $\Delta\varphi$ introduced by the respective laser pulses is the same for all interferograms. The perturbative description of the REMPI in Sec. II B shows that this phase difference is $\Delta\varphi = 2\varphi_{\mathrm{g}} - \varphi_{\mathrm{r}} - \varphi_{\mathrm{b}}$, where φ_{r}, φ_{g}, and φ_{b} are the relative optical phases of the red, green, and blue pulse, respectively [see Eq. (8)]. Therefore, the variation of $\Delta\varphi$ induces a uniform amplitude modulation of the interferograms in each channel. By scanning the relative optical phase φ_{g} and measuring energy-resolved photoelectron spectra we map out the amplitude modulation. In the following, these multiple energy-resolved interferograms in a phase-resolved measurement are denoted as the *phase map* to underscore both the relative optical phase as the key parameter in the measurement and the two-dimensional (2D) character of the result. Because the influence of the total optical phase difference $\Delta\varphi$ and the CEP is the same in each interferogram, relative phase shifts between the recorded modulations in the phase maps are exclusively attributed to differences in the MPI phases acquired in the corresponding pathways. Thus, in this trichromatic scheme the recorded phase maps provide direct access to the MPI phases via the observed phase shifts between the interferograms.

In the experiment we use temporally overlapping trichromatic PLP laser fields with central wavelengths of $\lambda_{\mathrm{r}} = 925$ nm (red band), $\lambda_{\mathrm{g}} = 797$ nm (green band), and $\lambda_{\mathrm{b}} = 708$ nm (blue band). The corresponding frequencies meet the frequency condition in Eq. (1). To study the MPI phase from resonant excitation, the red pulse is two-photon resonant with the 3*d* state [55] with the very small detuning $\hbar\delta_{\mathrm{r}}^{3d} = 2\hbar\omega_{\mathrm{r}} - \hbar\omega_{3d} \approx 10$ meV [see left magnification in Fig. 1(a)]. The spectral full width at half maximum (FWHM) of the red pulse is $\hbar\Delta\omega_{\mathrm{r}} \approx 30$ meV. In contrast, the MPI phases due to the transient population dynamics in the nonresonant 4*p* state are studied with the green ($\hbar\Delta\omega_{\mathrm{g}} \approx 60$ meV) and blue ($\hbar\Delta\omega_{\mathrm{b}} \approx 70$ meV) pulses. To eliminate the spectral intensity of the pulse at the transition frequency ω_{4p} [55] a mechanical blocker is inserted into the Fourier plane of our pulse shaper [see bottom right inset of Figs. 1(a) and 3(a)]. This procedure guarantees nonresonant excitation of the 4*p* state despite the small detuning. As a consequence, the spectrum of the green pulse is slightly asymmetric. The detunings of the green and blue pulse are $\hbar\delta_{\mathrm{g}}^{4p} = \hbar\omega_{\mathrm{g}} - \hbar\omega_{4p} \approx -50$ meV

and $\hbar\delta_b^{4p} = \hbar\omega_b - \hbar\omega_{4p} \approx 140$ meV, respectively [see right magnification in Fig. 1(a)]. Thus, our trichromatic scheme allows us to study MPI phases from excitation of two different intermediate states either via resonant or via red- ($\delta_g^{4p} < 0$) and blue-detuned ($\delta_b^{4p} > 0$) near-resonant pathways simultaneously.

In our theoretical model, the atom is described by a three-level system coupled to the continuum. The bound part consists of the ground state $|g\rangle$ and the two (near-)resonant intermediate states $|a\rangle$ and $|b\rangle$. The final state $|f\rangle$ with variable energy describes the free electron in the continuum (for details see Sec. II B). Due to the choice of the photon energies described above, the photoelectron interferograms in channels 1 and 3 are centered around the energies $\varepsilon_1 = 0.10$ eV and $\varepsilon_3 = 0.50$ eV. Generally, pathways composed of the same color combinations are energetically degenerate since they differ only by permutations. However, the transient population of the near-resonant $4p$ state introduces a spectral shift. In particular, since the green pulse is slightly red-detuned ($\delta_g^{4p} < 0$) with respect to the $4s \rightarrow 4p$ transition, its transient population follows the laser field envelope with an additional temporal phase. As a consequence, the photoelectron signals mapping the $4p$ state are slightly shifted upwards in energy. For the same reason, wave packets created via pathways starting with a blue photon ($\delta_b^{4p} > 0$) are slightly shifted downwards in energy. Thus, near but nonresonant excitation of the $4p$ state lifts the degeneracy of the involved frequency mixing contributions introducing an energetic splitting between the pathways with an initial green photon and those starting with a blue photon. In the interference channels 1 and 3 only the upper signals are observed since the multiplicity of the green-green-red and green-green-blue pathways favors the ones with a leading green photon. In channel 2 the red-green-blue pathway around $\varepsilon_2 = \hbar(\omega_r + \omega_g + \omega_b) = 0.31$ eV exhibits both an up-shifted signal centered around ε_2^{up} from the pathways with an initial green photon and a down-shifted signal centered around ε_2^{low} from the pathways with an initial blue photon. Note that this energetic separation is not to be confused with the Stark shift or the Autler-Townes splitting [56]. It is intensity independent and fully consistent with the perturbative description of the excitation (see Sec. II B and Appendix B for more details). Indeed, the energetic separation permits us to investigate both the red- and the blue-detuned near but nonresonant excitation of the $4p$ state, independently in a single interference channel [see bottom right inset of Fig. 1(a)]. In addition to the above-mentioned interferograms, we observe photoelectron signals at $\varepsilon_4 = 0.73$ eV and $\varepsilon_5 = 0.93$ eV. While the contribution at ε_4 originates from a frequency mixing pathway with two blue and one green photon, the one at ε_5 arises from the blue single-color pathway, depicted in Fig. 1(a). The former contribution is used for *in situ* temporal pulse characterization in Sec. III B. Figure 1(b) depicts a section through the *y-z* plane in polar representation and the energy-resolved spectrum obtained by integration over the angular coordinate of the measured PMD, highlighting the different contributions at ε_1-ε_5. Figure 1(c) shows the measured and Abel-inverted [57] three-dimensional (3D) PMDs of the three color-coded energetically nested $f(m=0)$-type interferograms (details see Sec. III). In this figure, the 3D PMDs of the contributions around ε_4 and ε_5 are omitted for clarity.

B. Perturbative description

In this section, we provide a theoretical description of the photoelectron wave packets created in the multichannel interferometry scheme. We focus on the spectral phases in the different interference channels introduced by the (near-)resonant excitation in the MPI processes. First, in Sec. II B 1 we introduce the trichromatic laser field in the temporal and spectral representation and derive a general expression for the photoelectron density in each interference channel. In Sec. II B 2, we use perturbation theory in a multilevel model to calculate the MPI phases in the relevant pathways.

1. Laser field and photoelectron distribution

The trichromatic PLP field is fully characterized by the scalar electric fields of each color. The total electric field (negative frequency analytic signal [58]) is therefore given by

$$E^-(t) = \sum_{j \in \{r,g,b\}} \mathcal{E}_j(t - \tau_j) e^{-i(\omega_j t - \varphi_j)}, \tag{3}$$

with the temporal pulse envelopes $\mathcal{E}_j(t)$ shifted in time by the delay τ_j, the central frequency ω_j, and the relative optical phase φ_j. In Eq. (3) the CEP of the field components is omitted because in our scheme the phase in the photoelectron spectrum introduced by the CEP is identical for all MPI pathways. The corresponding spectrum reads

$$\tilde{E}^-(\omega) = \sum_{j \in \{r,g,b\}} \tilde{\mathcal{E}}_j(\omega + \omega_j) e^{i(\varphi_i - (\omega + \omega_i)\tau_i)} \tag{4}$$

with the spectra of the envelopes $\tilde{\mathcal{E}}_j(\omega)$. Again, the three central frequencies ω_j are chosen such that the energy of two green photons equals the energy of one red plus one blue photon as described by Eq. (1). Simultaneous absorption of another red, green, or blue photon in both processes provides the photon energy to overcome the ionization potential and gives rise to the interference channels $l = 1, 2$, and 3, respectively [see visualization of the basic building block in the left inset of Fig. 1(a)]. Therefore, each interference channel l consists of two pathways **I** and **II** either with at least two green photons (**I**) or with at least one red and one blue photon (**II**). Both pathways contain a photon of the additional color x_l with $\boldsymbol{x} = [r, g, b]$, e.g., $x_1 = r$ for the additional red photon in channel 1. Due to the temporal overlap of the three colors [see Eq. (2)], every permutation of the involved photons gives rise to another MPI pathway. We can write both pathways as a set containing all permutations of the involved colors, i.e., $\mathcal{Q}_I^{(l)} = \text{Sym}(\{g, g, x_l\})$ and $\mathcal{Q}_{II}^{(l)} = \text{Sym}(\{r, b, x_l\})$ where Sym denotes the symmetric group. In general the resulting photoelectron interferogram in channel l is given by the superposition of all possible partial wave functions created via the pathways $\mathcal{Q}_I^{(l)}$ and $\mathcal{Q}_{II}^{(l)}$. However, as discussed in Sec. II A, the intermediate resonances in the potassium atom select the relevant pathways. Therefore, the description focuses on the superposition of relevant resonance-enhanced quantum path-

ways I $\in \mathcal{Q}_{\mathrm{I}}^{(l)}$ and II $\in \mathcal{Q}_{\mathrm{II}}^{(l)}$, where the ordering of the colors is fixed due to the resonances. As an example, we consider the superposition of the (ggb) and (brb) pathways in channel 3 (see Table I). Hence, we assume each interferogram $\Psi^{(l)}$ to be composed of two partial wave functions, i.e., $\Psi^{(l)} = \Psi_{\mathrm{I}}^{(l)} + \Psi_{\mathrm{II}}^{(l)}$. In the momentum representation, with the photoelectron momentum $\boldsymbol{k} = (k, \theta, \phi)$, these partial wave functions are written as [53,59]

$$\Psi_{\mathrm{I/II}}^{(l)}(\boldsymbol{k}) = c_{\mathrm{I/II}}^{(l)}(k) e^{i\varphi_{\mathrm{I/II}}^{(l)}} \psi_{3,0}(\theta, \phi)$$
$$= \left| c_{\mathrm{I/II}}^{(l)}(k) \right| e^{i(\chi_{\mathrm{I/II}}^{(l)}(k) + \varphi_{\mathrm{I/II}}^{(l)})} \psi_{3,0}(\theta, \phi), \quad (5)$$

where $\varphi_{\mathrm{I/II}}^{(l)}$ represents the acquired optical phase and $c_{\mathrm{I/II}}^{(l)}(k) = |c_{\mathrm{I/II}}^{(l)}(k)| e^{i\chi_{\mathrm{I/II}}^{(l)}(k)}$ denotes the photoelectron amplitude with the associated MPI phase $\chi_{\mathrm{I/II}}^{(l)}(k)$. Since the sum of the optical phases does not depend on the permutation of the colors, we find

$$\varphi_{\mathrm{I}}^{(l)} = 2\varphi_{\mathrm{g}} + \varphi_{x_l} \quad \text{and} \quad \varphi_{\mathrm{II}}^{(l)} = \varphi_{\mathrm{r}} + \varphi_{\mathrm{b}} + \varphi_{x_l} \quad (6)$$

for all pathways to the states $\Psi_{\mathrm{I/II}}^{(l)}$. Using Eq. (5) the resulting electron density of the photoelectron interferogram $\varrho^{(l)} = |\Psi^{(l)}|^2$ is given by

$$\varrho^{(l)}(\boldsymbol{k}) = \{O^{(l)}(k) + S^{(l)}(k) \cos[\gamma^{(l)}(k) + \Delta\varphi]\}$$
$$\times |\psi_{3,0}(\theta, \phi)|^2, \quad (7)$$

with the signal offset $O^{(l)}(k) = |c_{\mathrm{I}}^{(l)}(k)|^2 + |c_{\mathrm{II}}^{(l)}(k)|^2$ and the signal amplitude $S^{(l)}(k) = 2|c_{\mathrm{I}}^{(l)}(k)||c_{\mathrm{II}}^{(l)}(k)|$. In Eq. (7) the MPI phase difference in channel l is denoted by $\gamma^{(l)}(k) = \chi_{\mathrm{I}}^{(l)}(k) - \chi_{\mathrm{II}}^{(l)}(k)$ and the optical phase difference by $\Delta\varphi = \varphi_{\mathrm{I}}^{(l)} - \varphi_{\mathrm{II}}^{(l)}$. Using Eq. (6), the optical phase difference reads

$$\Delta\varphi = 2\varphi_{\mathrm{g}} - \varphi_{\mathrm{r}} - \varphi_{\mathrm{b}} \quad (8)$$

and is independent of the respective channel. Therefore, the phases between the interferograms are determined exclusively by the MPI phase differences, which is the characteristic feature of our multichannel interferometry scheme. Equation (7) describes the photoelectron interferograms in each channel as $f(m = 0)$-type wave packets [see Fig. 1(c)], which are periodically intensity modulated by variation of the relative optical phases φ_j. The modulation frequency is determined by the number of involved photons of the respective color. While the modulation is analogous to [53], the analysis of multiple interference channels, including different REMPI pathways, and the unambiguous mapping of the corresponding MPI phase differences extend the previous scheme. Specifically, the MPI phase differences manifest in the phase shifts $\gamma^{(l)}(k)$ of the modulation, which sensitively depend on the intermediate resonances in the MPI pathways.

2. Atomic MPI phases

In the next step, we discuss the influence of the atomic structure on the phases $\chi_{\mathrm{I/II}}^{(l)}(k)$ acquired in the MPI process by calculating the photoelectron amplitudes of the resonance-enhanced quantum pathways $\mathcal{R}_{\mathrm{I/II}}$, $\mathcal{G}_{\mathrm{I/II}}$, and $\mathcal{B}_{\mathrm{I/II}}$ (see Table I) using perturbation theory. For simplicity, we reduce the atomic excitation scheme in Fig. 1(a) to the three most relevant states, i.e., the ground state $|g\rangle$ and the two

(near-)resonant intermediate states $|a\rangle$ and $|b\rangle$ coupled to a final state $|f\rangle$ with variable energy in the continuum. This model system is excited by a single-color laser pulse with central frequency ω_0, as shown in Fig. 2(a). A detailed theoretical derivation of the population amplitudes is given in Appendix B. The generic scheme describes three-photon ionization similar to that in the experiment. The MPI process is subdivided into three steps. First, the state $|a\rangle$ (representing the $4p$ state) is nonresonantly excited from the ground state $|g\rangle$ (representing the $4s$ state). For a sufficiently large detuning of the laser central frequency ω_0 with respect to the transition frequency ω_{ga}, i.e., $\delta_1 = \omega_0 - \omega_{ga} \gg \Delta\omega$, implying $\tilde{\mathcal{E}}(\delta_1) \approx 0$, the resulting time-dependent population amplitude of state $|a\rangle$ can be approximated by [see Eq. (B10)]

$$c_a^{\mathrm{non}}(t) \propto \frac{e^{i\pi}}{\delta_1} e^{-i\hat{\delta}_1 t} \mathcal{E}(t). \quad (9)$$

Here $\hat{\delta}_1 = \delta_1 + \zeta$ denotes the reduced detuning which includes the phase shift ζ due to the intermediate resonance $|a\rangle$. This means that the time-dependent population instantaneously follows the driving electric field envelope—albeit with an additional temporal phase. For a Gaussian-shaped envelope, ζ can be estimated by (see Appendix B1b)

$$\zeta \approx -\frac{\Delta\omega^2}{4\ln(2)\,\delta_1}, \quad (10)$$

which explicitly depends on the detuning δ_1. Consequently, the phase shift induced by the intermediate state $|a\rangle$, i.e., the $4p$ state, is different for the red- and blue-detuned excitation and therefore responsible for the observed energy shift in channel 2. With the experimental parameters given in Sec. II A the effective energy shift between $\varepsilon_2^{\mathrm{up}}$ and $\varepsilon_2^{\mathrm{low}}$ can be estimated to be about $\hbar\Delta\zeta_{\mathrm{theo}} = \hbar\zeta_{\mathrm{g}} - \hbar\zeta_{\mathrm{b}} \approx 40\,\mathrm{meV}$. The experimental investigation of the energy shift in the interference channel 2 is presented in Sec. IV B.

Next, we consider the two-photon excitation of state $|b\rangle$ (representing the $3d$ state) via the transiently populated off-resonant state $|a\rangle$ and distinguish between two limiting cases. In the two-photon resonant case, when $\delta_2 = \hat{\delta}_1 + \omega_0 - \omega_{ba} = 0$, the population amplitude of $|b\rangle$ is given by [see Eq. (B11)]

$$c_b^{\mathrm{res}}(t) \propto \frac{e^{-i\frac{\pi}{2}}}{\delta_1} \int_{-\infty}^{t} \mathcal{E}^2(t')dt'. \quad (11)$$

In contrast, for nonresonant two-photon excitation, when $\delta_2 \neq 0$ and the two-photon resonance lies outside the bandwidth of the second-order laser spectrum implying $\tilde{\mathcal{E}}^{(2)}(\delta_2) \approx 0$, the amplitude of the state $|b\rangle$ reads [see Eq. (B15)]

$$c_b^{\mathrm{non}}(t) \propto \frac{e^{-i\delta_2 t}}{\delta_1 \delta_2} \mathcal{E}^2(t). \quad (12)$$

The third photon maps the population amplitude of $|b\rangle$ into the final continuum state $|f\rangle$ with photoelectron kinetic energy $\varepsilon = \hbar\omega_f - \hbar\omega_{\mathrm{IP}}$. This photoionization step leads to the final-state population amplitude of the free state $|f\rangle$:

$$c_f(t, \varepsilon) = -\frac{\mu_{fb}}{i\hbar} \int_{-\infty}^{t} c_b(t') \mathcal{E}(t') e^{-i\varpi(\varepsilon)t'} dt', \quad (13)$$

where $\varpi(\varepsilon) = \omega_0 - \omega_{fb}(\varepsilon) = \omega_0 - \frac{\varepsilon}{\hbar} + \omega_b - \omega_{\mathrm{IP}}$. Photoionization via the two-photon resonant pathway yields the final
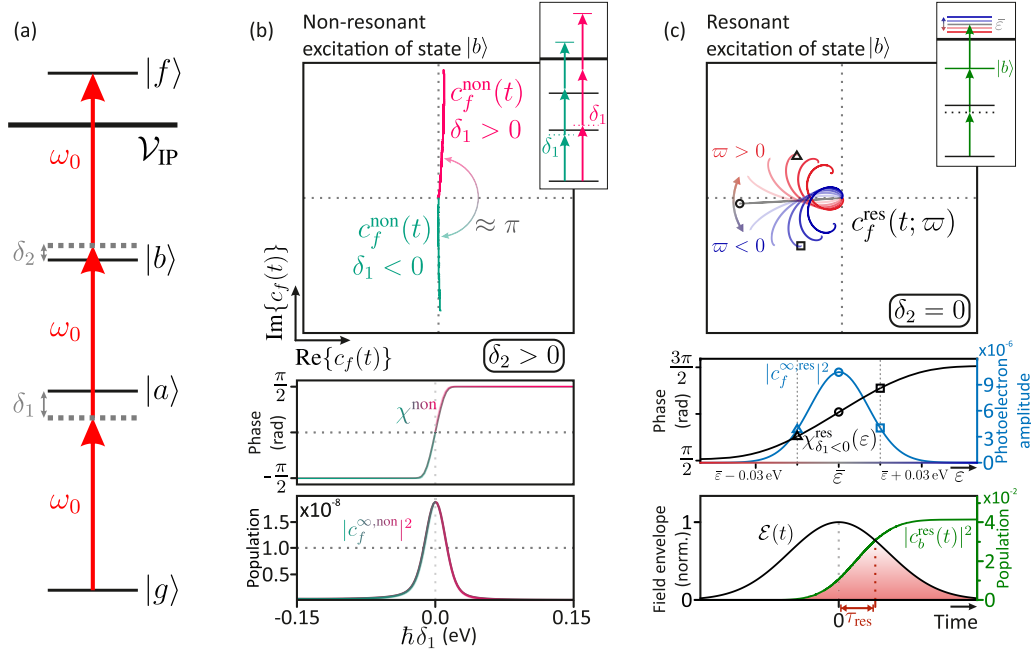
FIG. 2. (a) Three-level system with the states $|g\rangle$, $|a\rangle$, and $|b\rangle$ coupled to the continuum state $|f\rangle$ for the excitation by a laser field with the frequency ω_0 and an intensity FWHM of $\Delta t = 90$ fs. The detunings between the exciting laser field and the respective states are δ_1 and δ_2. (b) Time-dependent photoelectron amplitude $c_f^{\text{non}}(t)$ in the complex plane representation for nonresonant excitation of the state $|b\rangle$ and different signs of the detuning δ_1 (upper frame). Phase $\chi^{\text{non}} = \arg\{c_f^{\infty,\text{non}}\}$ and photoelectron amplitude $|c_f^{\infty,\text{non}}|^2$ as a function of the detuning δ_1 (lower frames). (c) Time-dependent population amplitudes $c_f^{\text{res}}(t;\varpi)$ for different values of $\varpi(\varepsilon)$ assuming resonant excitation of the state $|b\rangle$ and $\delta_1 < 0$ (upper frame). The middle frame shows the photoelectron amplitude $|c_f^{\infty,\text{res}}|^2$ and corresponding MPI phase $\chi_{\delta_1<0}^{\text{res}}$ as a function of ε. The bottom frame illustrates the physical picture of the resonance-induced photoionization time delay, explained by windowing of the temporal field envelope $\mathcal{E}(t)$ with the time-dependent population amplitude of $|b\rangle$.

$(t \rightarrow \infty)$ amplitude [see Eq. (B18)]:

$$c_f^{\infty,\text{res}}(\varepsilon) \propto \frac{1}{\delta_1}\left(\tilde{\mathcal{E}}^{(2)}(0)\tilde{\mathcal{E}}[\varpi(\varepsilon)] - 2i\mathcal{E}^2(0)\frac{\partial\tilde{\mathcal{E}}}{\partial\omega}[\varpi(\varepsilon)] \right)$$
$$= \left|c_f^{\infty,\text{res}}(\varepsilon)\right| e^{i\chi^{\text{res}}(\varepsilon)}. \qquad (14)$$

In contrast, the nonresonant pathway yields the amplitude of [see Eq. (B22)]

$$c_f^{\infty,\text{non}}(\varepsilon) \propto \frac{e^{i\frac{\pi}{2}}}{\delta_1\delta_2}\tilde{\mathcal{E}}^{(3)}[\varpi(\varepsilon) + \delta_2]$$
$$= \left|c_f^{\infty,\text{non}}(\varepsilon)\right| e^{i\chi^{\text{non}}}. \qquad (15)$$

Equations (14) and (15) show that for a positive detuning $\delta_2 \geqslant 0$, as in the experiment, and a symmetric and real-valued spectral envelope, the MPI phases are determined by the sign of the detuning δ_1, i.e.,

$$\chi^{\text{res}}(\varepsilon) = \begin{cases} \pi + \xi(\varepsilon)\,; \ \delta_1 < 0 \\ \xi(\varepsilon)\,; \ \delta_1 > 0 \end{cases}, \qquad (16)$$

$$\chi^{\text{non}} = \begin{cases} 3\pi/2\,; \ \delta_1 < 0 \\ \pi/2\,; \ \delta_1 > 0 \end{cases}. \qquad (17)$$

In Eq. (16), $\xi(\varepsilon)$ represents the temporally accumulated phase due to the resonant excitation of the 3d state which is discussed in the following. Since the population buildup in the resonant state occurs on the time scale of the pulse duration, the reference partial photoelectron wave packet, created by nonresonant ionization, accumulates its time-evolution phase in the continuum during the formation of the photoelectron

interferogram. Thus, the time delay introduced by the population dynamics in the resonant 3d state manifests in a linear spectral phase between the 3d-resonant pathway $\mathcal{R}_{\text{II}}$ and the nonresonant pathway $\mathcal{R}_{\text{I}}$. For a Gaussian-shaped pulse envelope the phase can be approximated by $\xi(\varepsilon) = \tau_{\text{res}}\varpi(\varepsilon)$ with (see Appendix B for details)

$$\tau_{\text{res}} \approx \sqrt{\frac{\ln(2)}{\pi}}\frac{4}{\Delta\omega} = \frac{\Delta t}{\sqrt{\ln(2)\pi}}, \qquad (18)$$

where Δt represents the pulse duration. An experimental investigation of the resonance-induced time delay, in terms of a linear spectral phase in the interference channel 1, is demonstrated in Sec. IV B.

To verify the MPI phases predicted by the perturbation theory, we numerically solve the TDSE for the model system depicted in Fig. 2(a). The numerical implementation is described in previous work [15,60] and Appendix A. The results of the simulation for the nonresonant and the resonant excitation of state $|b\rangle$ are depicted in Figs. 2(b) and 2(c), respectively. In the nonresonant case, the time-dependent photoelectron amplitudes represented in the complex plane describe almost straight lines as shown in the upper frame of Fig. 2(b). Each line is rotated by $\pm\pi/2$ with respect to the real axis, where the lower sign corresponds to $\delta_1 < 0$ (red-detuned) and the upper sign to $\delta_1 > 0$ (blue-detuned), as predicted by Eq. (17). This observation agrees with the variation of the MPI phase χ^{non} from $\chi^{\text{non}} = -\frac{\pi}{2}$ to $\frac{\pi}{2}$ as the detuning varies from $\hbar\delta_1 = -0.15$ to 0.15 eV as shown

in the middle frame of Fig. 2(b). The bottom frame depicts the final population $|c_f^{\infty,\text{non}}|^2$ as a function of the detuning δ_1, showing a bell-shaped profile centered around $\delta_1 \approx 0$. Note that δ_2 is a function of δ_1.

Next, we consider two-photon resonant excitation of the state $|b\rangle$, with $\delta_1 < 0$. Since resonant excitation leads to an energy-dependent MPI phase $\chi_{\delta_1<0}^{\text{res}}(\varepsilon)$ according to Eq. (16), we investigate the final-state amplitude c_f^{res} as a function of the photoelectron kinetic energy. The upper frame of Fig. 2(c) shows the time evolution of $c_f^{\text{res}}(t;\varpi)$ in the complex plane for different energies in the photoelectron continuum, i.e., different values of $\varpi(\varepsilon)$ (red, blue, and gray lines). The red and blue shaded curves illustrate the corresponding time-dependent amplitudes for different values of $\varpi \neq 0$. The nearly horizontal gray line is connected to the final phase value of $\chi^{\text{res}}(\bar{\varepsilon}) = \pi$ [see Eq. (16)], since the phase introduced by the population dynamics $\xi(\bar{\varepsilon})$ vanishes. In contrast, for $\varepsilon \neq \bar{\varepsilon}$, the time evolution of the energy-dependent amplitude describes a curve moving either upwards ($\varpi > 0$, red lines) or downwards ($\varpi < 0$, blue lines) on the imaginary axis. The middle frame of Fig. 2(c) depicts the energy-resolved photoelectron amplitude $|c_f^{\infty,\text{res}}|^2$ (blue) and phase $\chi_{\delta_1<0}^{\text{res}}(\varepsilon)$ (black). Here, the symbols (circle, square, and triangle) indicate the end points of the final-state populations shown in the upper frame. In the region of a nonvanishing photoelectron amplitude $|c_f^{\infty,\text{res}}|^2$, the phase exhibits a linear behavior, confirming the assumption of $\xi(\varepsilon) \approx \tau_{\text{res}}\varpi(\varepsilon)$. The bottom frame shows a physical picture of the resonance-induced ionization time delay due to the windowing of the Gaussian-shaped temporal field envelope $\mathcal{E}(t)$ with the time-dependent population amplitude of the state $|b\rangle$. While nonresonant excitation and ionization follows the field envelope almost instantaneously [see Eq. (9)], resonant ionization introduces a temporal shift in the order of the pulse duration according to Eq. (18), corresponding to a linear spectral phase.

III. EXPERIMENT

In this section we describe our experimental setup and strategy. The trichromatic fields are generated using white light polarization pulse shaping [53,61,62] and we apply photoelectron velocity map imaging (VMI) [63] to measure energy- and angle-resolved photoelectron spectra.

A. Experimental setup

The trichromatic experimental scheme is based on our setup previously reported in [53]. Briefly, trichromatic pulse shaping is implemented using a home-built $4f$ polarization pulse shaper [61] employing a dual-layer liquid crystal spatial light modulator (LC-SLM). The shaper is specifically adapted to the white light supercontinuum (WLS) [62] generated by seeding a neon-filled hollow-core fiber compressor with 20-fs pulses ($\lambda_c = 790$ nm) from an amplified laser system (Femtolasers Femtopower HR 3 kHz). Employing a custom broadband p polarizer (Codixx colorPol) in the Fourier plane of the shaper, we generate a PLP trichromatic field [see inset in Fig. 3(a)] by spectral amplitude and phase modulation. To individually advance or delay the pulses of different colors in time, we apply linear spectral phase functions to the LC-SLM.
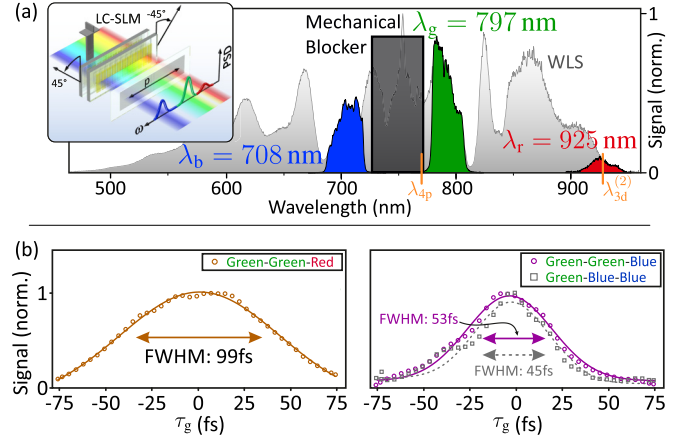

FIG. 3. (a) Measured trichromatic spectrum together with the WLS. The inset shows a schematic of the pulse shaper setup with a broadband p polarizer and the mechanical blocker in the Fourier plane to eliminate resonant excitation of the $4p$ state. (b) Energy sections of the time-resolved measurements on the *green-red* (left) and *green-blue* (right) frequency mixing signals from *in situ* temporal pulse characterization (circles and squares) together with Gaussian fits (solid and dashed lines) and corresponding FWHMs.

Owing to the common-path geometry of the shaper-based scheme, the generated trichromatic pulse sequences are inherently phase locked allowing for high-precision time- and phase-resolved measurements [64]. The measured spectrum of the trichromatic field is shown in Fig. 3(a) along with the input WLS. The central wavelength of the red pulse is set to $\lambda_r = 925$ nm (red), i.e., tuned to the two-photon resonance of the $3d$ state, indicated by the right vertical orange line. The central wavelengths of the green and blue pulses are set to $\lambda_g = 797$ nm and $\lambda_b = 708$ nm, respectively. Spectral components resonant with the $4p$ state are eliminated by employing a mechanical blocker [see inset in Fig. 3(a)] in the Fourier plane between the blue and green component (see also the left vertical orange line). The spectral bandwidths of the red, green, and blue bands are set to $\Delta\omega_r = 50$ mrad/fs, $\Delta\omega_g = 90$ mrad/fs, and $\Delta\omega_b = 100$ mrad/fs (FWHM of the intensity), corresponding to bandwidth-limited pulse durations of $\Delta t_r \approx 55$ fs, $\Delta t_g \approx 32$ fs, and $\Delta t_b \approx 28$ fs, respectively, assuming Gaussian-shaped envelopes. Using a spherical mirror, the trichromatic pulse is focused into the interaction region of a VMI spectrometer filled with potassium vapor from a dispenser source. The peak intensity of the temporally overlapping trichromatic field in the interaction region is estimated to be on the order of $I_0 \approx 5 \times 10^{12}$ W/cm^2. Abel inversion of the recorded 2D VMI images, using the pBasex algorithm [57], yields the PMD of the created photoelectron wave packets. Angle integration and energy calibration [65] of the PMD leads to the energy-resolved photoelectron spectra shown in Fig. 1(b).

B. Experimental preparation and characterization

In this section, we describe how we prepare and characterize the shaper-generated trichromatic field for the experiment. To maximize the interference contrast in all three

interference channels l [see Fig. 1(a)], we optimize the temporal overlap and the amplitudes of the three colors together with the spectral overlap of the partial photoelectron wave packets in each channel. First, to compress the WLS in time, we use a shaper-based evolutionary optimization procedure to maximize the second harmonic yield of the WLS from a thin β-barium borate crystal (Eksma Optics, cutting angle $\theta = 29.2°$, 5-μm thickness) [66,67]. Subsequently, an initial trichromatic spectrum is sculpted from the compressed WLS by spectral amplitude modulation. In the second step, the frequency mixing contributions in the second harmonic signal of the trichromatic field are maximized by shaper-based pairwise optimization of the second- and third-order dispersion. The refined and temporally compressed trichromatic field is then focused into the interaction region of the VMI spectrometer to perform an additional *in situ* temporal characterization and an iterative spectral optimization of the sculpted field in the laser focus. To this end, we iteratively adjust the amplitude and central wavelength of the individual colors to maximize the contrast of the photoelectron interferograms in phase maps [53]. For the final characterization of the temporal overlap we perform bichromatic time-resolved measurements by varying the time delay τ_g of the green pulse with a step size of $\delta\tau_g = 3.75\,\text{fs}$ and record the *green-red* and the *green-blue* photoelectron frequency mixing contributions. Figure 3(b) shows sections from these time-resolved measurements at kinetic energies ε_1 (left) as well as ε_3 and ε_4 (right) together with Gaussian fits (solid and dashed lines). The results show a maximal temporal overlap of the green and red pulse at $1.7(8)\,\text{fs}$ and of the green and blue pulse at $-3.5(13)\,\text{fs}$, i.e., within the temporal step size, ensuring efficient frequency mixing. By applying the procedure described in [53] we obtain pulse durations of $\Delta t_r = 50(8)\,\text{fs}$, $\Delta t_g = 49(12)\,\text{fs}$, and $\Delta t_b = 29(12)\,\text{fs}$ from the measured FWHMs shown in Fig. 3(b). The values for the red and blue pulse are in good agreement with the estimated bandwidth-limited pulse durations from Sec. III A. The retrieved pulse duration of the green component is slightly larger than the value obtained in Sec. III A, which is attributed to the mechanically blocked edge of the green spectral component resulting in a non-Gaussian pulse shape. Overall, the results confirm a flat spectral phase of the trichromatic field.

C. Experimental strategy

To extract the MPI phase differences from the measured photoelectron interferograms, the experiment consists of two parts. In Sec. IV A, we describe the energy- and phase-resolved measurements, i.e., phase maps. In the experiment, we vary the relative optical phase of the green pulse φ_g and measure photoelectron spectra which are energy calibrated [65] and angularly integrated,

$$\varrho_{\text{int}}(\varepsilon) = \int_0^{2\pi} \varrho(\varepsilon, \theta) d\theta, \tag{19}$$

yielding the kinetic energy-resolved phase maps $\varrho_{\text{int}}(\varepsilon, \varphi_g; \varphi_r + \varphi_b)$, with $\varepsilon = \frac{(\hbar k)^2}{2m_e}$. Changing the phase of the

blue pulse by π inverts the measured phase maps. In Sec. IV B this inversion is used to remove the phase-insensitive background. To this end, we calculate the phase contrast map $\mathcal{C}(\varepsilon, \varphi_g)$ analogously to [53] by subtracting two normalized measured phase maps with an effective phase difference of $|\varphi_r + \varphi_b| = \pi$, i.e.,

$$\mathcal{C}(\varepsilon, \varphi_g) = \varrho_{\text{int}}(\varepsilon, \varphi_g; 0) - \varrho_{\text{int}}(\varepsilon, \varphi_g; \pi)$$
$$\propto \cos(\gamma^{(l)}(\varepsilon) + 2\varphi_g). \tag{20}$$

Due to this difference between two inverted phase maps, the phase contrast map emphasizes the contrast of the measured phase-resolved interferograms and thus reveals even subtle imprints of the MPI phases in the recorded photoelectron spectra. In particular, the splitting of channel 2 into an upper and a lower contribution corresponding to the red- and blue-detuned excitation of the $4p$ state can be clearly seen. In addition, it directly maps the spectral phase due to the resonant excitation of the $3d$ state in the interference channel 1.

IV. RESULTS AND DISCUSSION

In Sec. IV A, we present the φ_g-resolved phase maps and demonstrate their inversion by changing the optical phase of the blue pulse from $\varphi_b = 0$ to $-\pi$. In Sec. IV B, we remove the phase-insensitive background by calculating the phase contrast map $\mathcal{C}(\varepsilon, \varphi_g)$ [see Eq. (20)] and retrieve the MPI phases induced by the intermediate states $4p$ and $3d$.

A. Phase control of the photoelectron interferograms

First, we investigate the phase control of the photoelectron interferograms in φ_g-resolved phase maps $\varrho_{\text{int}}(\varepsilon, \varphi_g; \varphi_r + \varphi_b)$. In Figs. 4(a) and 4(b) the simulated and measured phase maps $\varrho_{\text{int}}(\varepsilon, \varphi_g; \pi)$ are compared. The observed phase dependence validates the scheme by showing that the same optical phase is imprinted in all interferograms [see Eq. (7)]. In the experiment, we vary $\varphi_g \in [-\pi, \pi]$ with a step size of $\delta\varphi_g = \frac{2\pi}{40}$ and set the phases of the red and blue pulse to $\varphi_r = \pi$ and $\varphi_b = 0$, respectively. The upper frame of Fig. 4(b) depicts the measured phase map which shows the three energetically separated interference channels centered around ε_1, ε_2, and ε_3 in an energy window of $\varepsilon \in [0, 0.6]\,\text{eV}$. In accordance with the theoretical description in Sec. II B, each channel is strongly amplitude modulated with a periodicity of π; however, each with an individual phase offsets due to MPI phases. The π periodicity is due to the fact that effectively two green photons contribute to each interferogram, resulting in a modulation period of $\frac{2\pi}{2} = \pi$ [see Eq. (8)]. The results in channel 2 show small energetic oscillations of the signal attributed to the two slightly shifted contributions discussed in Sec. II A. These two contributions, which are hardly distinguishable at this point, are more clearly visible in the phase contrast map and, therefore, they will be discussed in detail in Sec. IV B. First, we analyze the modulations in channels 1 and 3 around ε_1 and ε_3. To quantitatively evaluate the modulation of the photoelectrons in the channels 1 and 3, we take sections through the phase maps along the phase axis at ε_1 (orange squares) and ε_3 (violet circles). These sections are shown in the bottom frame of Fig. 4(b) together with cosine fits through the data (orange dashed and violet solid lines). The inversion of the phase map
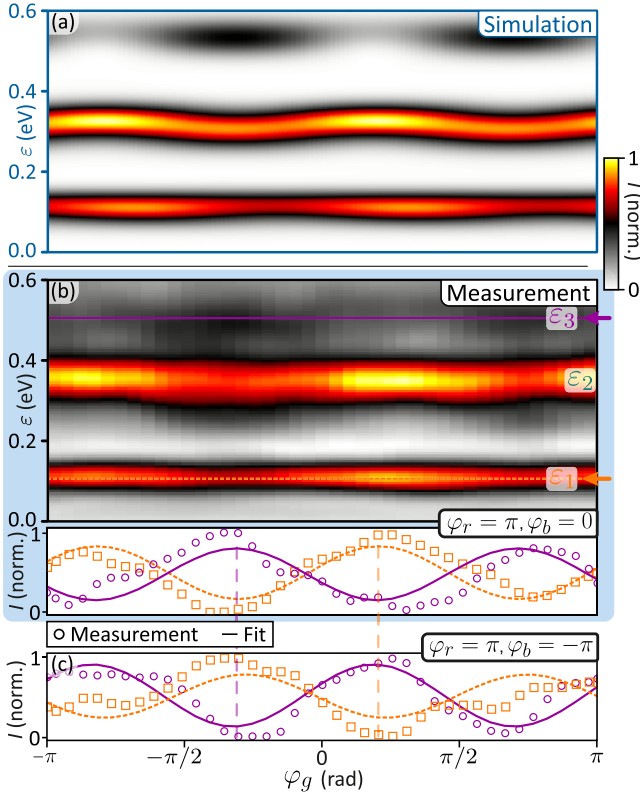
FIG. 4. Simulated and measured phase maps of photoelectron interferograms from multichannel interferometry by varying the phase of the green pulse $\varphi_g \in [-\pi, \pi]$. (a) Simulated phase map obtained by numerical solution of the TDSE for the perturbative interaction of a three-level atom with the trichromatic field having optical phases of $\varphi_r = \pi$, $\varphi_b = 0$. (b) Measured phase map for $\varphi_r = \pi$, $\varphi_b = 0$ with a step size of $\delta\varphi_g = \frac{2\pi}{40} \approx 0.16$ rad, showing the three energetically separated interference channels around $\varepsilon_1 - \varepsilon_3$. Bottom frame: Section through the phase maps along the phase axis at ε_1 (orange) and ε_3 (violet) to emphasize the modulation. (c) Same as the bottom frame of panel (b) but for $\varphi_r = \pi$, $\varphi_b = -\pi$. The vertical dashed lines serve as a guide to the eye for visualization of the phase shift between the orange and violet lines, respectively.

is demonstrated by setting $\varphi_b = -\pi$. The experimental result of the inversion is shown in Fig. 4(c). The orange (channel 1) as well as violet lines (channel 3) in Fig. 4(c) and the bottom frame of Fig. 4(b) are both phase shifted about 3.2(3) rad, confirming the inversion of the interference patterns, taking into account the error of the fit parameters. Minor imperfections of the inverted phase map are attributed to diffraction on the discrete phase mask of the SLM [68,69]. The phase shifts between the modulations due to MPI phase differences in all channels will be discussed in Sec. IV B.

Our interpretation of the experimental findings is confirmed by the simulated phase map in Fig. 4(a) for $\varphi_r = \pi$, $\varphi_b = 0$, which is in good agreement with the measured phase map in the upper frame of Fig. 4(b). In the simulation, we consider a three-level system consisting of the states $4s$, $4p$, and $3d$ (similar to Sec. II B and Appendix A) which interacts with a sequence of three Gaussian-shaped pulses similar to those used in the experiment (see Sec. III). By numerically solving the TDSE for the three-level system, we obtain the

bound-state population dynamics. Subsequently, we calculate the energy-resolved photoelectron spectra using time-dependent perturbation theory (see, e.g., [70] for details).

B. MPI phase retrieval

In this section, we study the phase shifts between the interferograms observed in the different interference channels. These phase shifts originate from the MPI phases acquired in the corresponding photoionization processes. For the background-free determination of the phase shifts in Fig. 4, we calculate the phase contrast maps $\mathcal{C}(\varepsilon, \varphi_g)$ according to Eq. (20) from the phase maps presented in Sec. IV A. The simulated and experimental phase contrast maps are depicted in Figs. 5(a) and 5(b), respectively. To highlight the measured interferograms in Fig. 5(b), we apply super-Gaussian filters to blank the space between the regions of interest. The phase contrast map reveals the splitting of channel 2 which is barely visible in the phase map shown in Fig. 4(b). The two contributions are indicated by the petrol-blue dashed and green dash-dotted lines at $\varepsilon_2^{up} = 0.35$ eV and $\varepsilon_2^{low} = 0.28$ eV, respectively. In this representation, the maxima have a spectral separation of about $\hbar\Delta\zeta_{meas} \approx 70$ meV which exceeds the theoretically expected separation of $\hbar\Delta\zeta_{theo} \approx 40$ meV from Eq. (10) (see Sec. II B). The deviation is explained by the near-resonant excitation $\delta_1 \approx \Delta\omega$ in the experiment, in contrast to the assumption of $\delta_1 \gg \Delta\omega$ in the theoretical description. However, since the mechanical blocker in the Fourier plane produces a strongly non-Gaussian optical spectrum with vanishing intensity at resonance, the assumption $\tilde{\mathcal{E}}(\delta_1) \approx 0$ is still valid. Moreover, the choice of frequencies in the experiment leads to a slight energetic separation in the frequency mixing and the green single-color signals of 20 meV. The results show that both contributions in channel 2 exhibit a π-periodic oscillation similar to those observed in channel 1 and 3 (see discussion in Sec. IV A). Again, for quantitative evaluation of the MPI phases, we take energy sections through the phase contrast map along the φ_g axis. The sections at ε_3 (violet circles), ε_2^{up} (petrol-blue circles), and ε_2^{low} (green circles) are shown in Figs. 5(c)–5(e) along with cosine fits through the data (lines). The phases $\gamma^{(l)}$ extracted from the channels $l = 2$ (up and low) and 3 provide the MPI phase difference

$$\Delta\gamma^{(l-l')} = \gamma^{(l)} - \gamma^{(l')} \qquad (21)$$

between two channels l and l'. To rationalize the extracted phase differences $\Delta\gamma$, we discuss the values $\Delta\gamma^{(3-2,low)}$ and $\Delta\gamma^{(2,up-2,low)}$ by comparing them with the theoretical results, starting with $\Delta\gamma^{(3-2,low)}$.

In both the channels 3 and (2, low), two ionization pathways interfere, one of which originates from a blue-detuned near-resonant transition, the other from a red-detuned near-resonant transition. Consequently, the MPI phase difference between the interference channel 3 and the lower part of channel 2 is expected to vanish (see Table I), in good agreement with the measured phase difference of $\Delta\gamma^{(3-2,low)} = 0.0(2)$ rad.

Next, we investigate the MPI phase difference $\Delta\gamma^{(2,up-2,low)}$. In multichromatic photoionization, different final states are addressed with different combinations and
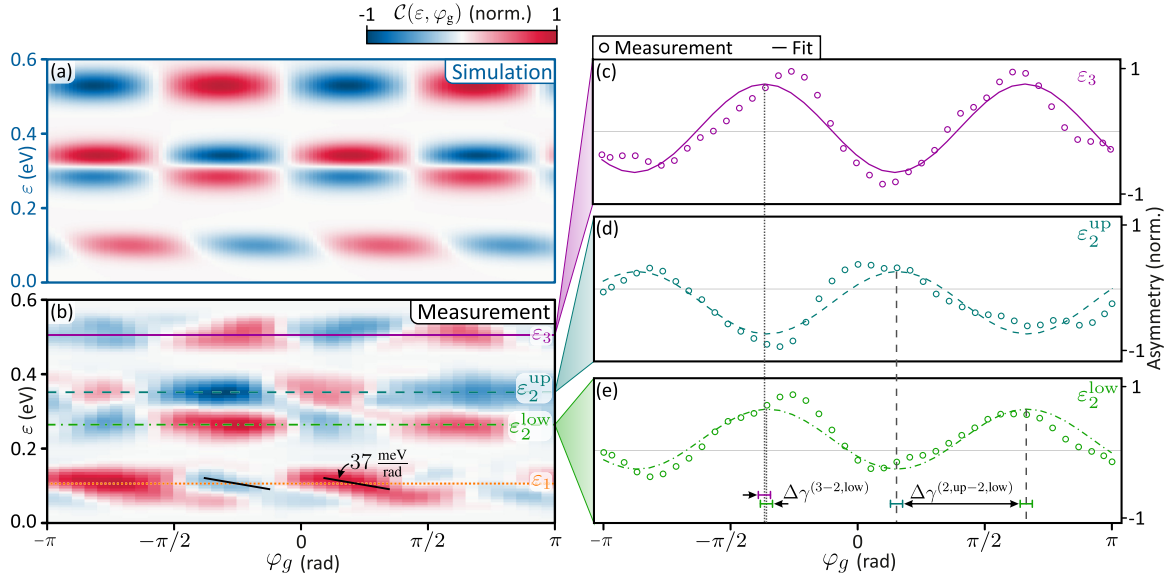
FIG. 5. Simulated (a) and measured (b) phase contrast maps $\mathcal{C}(\varepsilon, \varphi_g)$ with $\varphi_r = \pi$ extracted from inverting the phase maps by changing the phase of the blue pulse from $\varphi_b = 0$ to $-\pi$. (a) Simulated phase contrast map based on the numerical results described in Sec. IV A, shown in Fig. 4(a). (b) Measured phase contrast map calculated from the results of Sec. IV A, shown in Fig. 4(b). The different channels are indicated by horizontal lines. To emphasize the interference channels, we apply super-Gaussian filters to blank the space between the regions of interest. (c–e) Sections through the measured phase contrast map (circles) at the kinetic energies of ε_3 (c), $\varepsilon_2^{\mathrm{up}}$ (d), and $\varepsilon_2^{\mathrm{low}}$ (e) together with cosine fits through the data (lines). The MPI phase differences $\Delta\gamma$ are highlighted by vertical dashed black lines through the frames (c)–(e) together with their associated color-coded error bars.

permutations of the colors in the laser field. However, the pathways to create the photoelectrons in the interference channel 2, i.e., $\mathcal{G}_{\mathrm{II}}^{\mathrm{up}}$ at $\varepsilon_2^{\mathrm{up}}$ and $\mathcal{G}_{\mathrm{II}}^{\mathrm{low}}$ at $\varepsilon_2^{\mathrm{low}}$, differ only in the permutations of the photons—albeit with the common reference pathway $\mathcal{G}_{\mathrm{I}}$ [see Sec. II A and Fig. 1(a)]. Therefore, the phase difference within the interference channel 2 is uniquely determined by the MPI phases introduced by the red-detuned (upper signal) and blue-detuned (lower signal) $(1 + 2)$ REMPI processes. To analyze the dynamics, we first note that the red or blue detuning of the field corresponds to an opposite sign of δ_1. As a consequence, the two contributions in the interference channel 2 map the transient population dynamics of the $4p$ state but with opposite signs in the amplitude $1/\delta_1$ and in the time-dependent phase $\hat{\delta}_1 t$ as described by Eq. (9). While the sign change in the phase explains the previously described energetic splitting, the different signs of the amplitudes lead to a theoretical MPI phase difference of $\Delta\gamma_{\mathrm{theo}}^{(2,\mathrm{up}-2,\mathrm{low})} = -\pi$ [see Fig. 2(b) and Table I]. The measured MPI phase difference of $\Delta\gamma^{(2,\mathrm{up}-2,\mathrm{low})} = -3.1(2)\,\mathrm{rad}$ confirms the above physical picture.

Finally, we discuss the interference pattern observed in channel 1 by analyzing the phase contrast map shown in Fig. 5. Both, the measured and the simulated phase contrast maps in Figs. 5(a) and 5(b) show a pronounced spectral shearing around ε_1 corresponding to an approximately linear spectral phase. Following the discussion in Sec. II B, we explain the linear spectral phase by identifying a time delay in the resonant photoionization. The $(2 + 1)$ REMPI pathway $\mathcal{R}_{\mathrm{II}}$ in channel 1 consists of the two-photon resonant excitation of the $3d$ state with the red pulse and the one-photon

ionization with the blue pulse. The physical picture to rationalize the time delay is illustrated in the bottom frame of Fig. 2(c). Due to the two-photon resonance, the time evolution of the population amplitude of the $3d$ state has a sigmoidal shape. Since the REMPI process is characterized by the ionization of the resonant $3d$ state, the product of the temporal envelope of the ionizing pulse and the time-dependent population amplitude appears in the perturbative description of the photoionization in Eq. (13). Hence, the temporal envelope of the ionizing blue pulse $\mathcal{E}_b(t)$ is windowed by the sigmoidal-shaped population amplitude $c_b^{\mathrm{res}}(t)$. The windowing results in a time delayed formation of the photoelectron wave packet from $(2 + 1)$ REMPI with respect to the temporal pulse envelope. The interference of the time delayed wave packet from the resonant $(2 + 1)$ REMPI pathway $\mathcal{R}_{\mathrm{II}}$ with the wave packet from the near-resonant $(1 + 2)$ REMPI pathway $\mathcal{R}_{\mathrm{I}}$ in channel 1 gives rise to the spectral shearing in the phase map, similar to [27,53,71]. However, in contrast to previous results, here the shearing originates from a time delay due to the resonant excitation rather than an optical delay. Assuming a Gaussian-shaped temporal pulse envelope $\mathcal{E}(t)$, the associated linear spectral phase can be approximated around the center of the signal $[\varpi(\bar{\varepsilon}) = 0]$ by $\xi(\varepsilon) \approx -\frac{\tau_{\mathrm{res}}}{\hbar}\varepsilon + \xi_0$ with the resonance-induced time delay τ_{res} from Eq. (18) (see Appendix B 3 a for a detailed discussion). For the field parameters used in the experiment (Sec. III B) we calculate a delay of $\tau_{\mathrm{res}} \approx 19\,\mathrm{fs}$ which corresponds to a slope of $37\,\mathrm{meV/rad}$. This slope derived from theory is indicated in Fig. 5(b) and in good agreement with the observed shearing in the phase contrast map of channel 1. Our results show that multichannel interferometry with temporally overlapping trichromatic fields allows

one to unambiguously determine the MPI phases acquired in REMPI processes.

V. SUMMARY AND CONCLUSION

In this paper, we presented the unambiguous determination of quantum phases in MPI dynamics using a multichannel photoelectron interferometry scheme. We demonstrated the scheme on the MPI of potassium atoms with temporally overlapping parallel linearly polarized trichromatic fields. By appropriate choice of the optical frequencies so that $2\omega_g \approx \omega_r + \omega_b < \omega_{IP}$, the photoelectron wave packets overlap in different interference channels and create three energetically separated interferograms. These interferograms are sensitive to both the optical and the MPI phases acquired along the different MPI pathways. Due to the design of the scheme, the optical phase is identical in all interferograms. Therefore, the measured phase shifts directly revealed the MPI phases introduced by the MPI dynamics in the different interference channels. Specifically, the red pulse was tuned to the two-photon $4s \rightarrow\rightarrow 3d$ transition, opening a $(2 + 1)$ REMPI pathway via ionization with the blue pulse. The green and the blue pulse were tuned close to the $4p$ resonance with opposite detunings to implement two different $(1 + 2)$ REMPI pathways via trichromatic frequency mixing. We observed high-contrast phase-shifted intensity modulations in the photoelectron interferograms by varying the green pulse's relative phase. By introducing an optical phase of $-\pi$ to the blue pulse, the interferograms were inverted and used to remove the phase-insensitive background. Analysis of the background-free interferograms unambiguously revealed the MPI phases introduced by the intermediate resonances.

The measured interferograms showed that the MPI phases manifest in three different ways: First, we observed an energetic splitting of the photoelectron interferograms from red- and blue-detuned $(1 + 2)$ REMPI. Although interferograms from frequency mixing pathways, consisting of different photon permutations, should be energetically degenerate, we demonstrated that the near but nonresonant excitation of the intermediate $4p$ state lifts this degeneracy. Second, we observed constant phase shifts of π both between the split interferograms within one interference channel and between interferograms of different interference channels. These phase shifts between the different $(1 + 2)$ REMPI signals originate from population amplitudes with opposite signs. Finally, we demonstrated that the photoionization time delay through the resonant excitation of the $3d$ state in the $(2 + 1)$ REMPI pathway gives rise to a linear spectral phase in the photoelectron interferograms observed as a pronounced spectral shearing. All observations were analyzed using an analytic perturbative description and numerical simulations of a trichromatic driven three-level system coupled to the continuum.

In conclusion, we demonstrated that our shaper-based trichromatic multichannel interferometry scheme is a powerful tool to measure the phase of ultrafast free electron wave packets. We showed that the resonance-induced photoionization time delay associated with a linear spectral phase is a general feature of processes involving a resonant intermediate state. For example, the structure of bichromatic photoelectron vortices as reported in [28,72,73] is affected

by the intermediate resonances. Currently, we investigate further applications of multichromatic free electron vortex spectroscopy with polarization-tailored trichromatic fields in our laboratories, where information on the ionization and bound dynamics is imprinted in the angular part of the photoelectron momentum distribution. In addition, multichannel interferometry in 2D spectroscopy [74] on atomic [75–77] and molecular [78] systems or nanostructures [79] gives rise to multiple energetically separated 2D spectra in one measurement, containing rich spectroscopic information on different aspects of the dynamics. In general, our results show that multicolor schemes open up entirely new perspectives for the measurement and coherent control of ultrafast quantum dynamics if we succeed in harnessing the great variety of interference pathways by a suitable design of the experiment.

ACKNOWLEDGMENTS

APPENDIX A: GENERIC THREE-LEVEL SYSTEM

For the convenience of the reader and to introduce our notation, this Appendix provides a detailed description of the multichannel interferometry scheme studied in the experiment. In this section, we describe the perturbative excitation of a generic three-level atom by a laser electric field $E(t) = \mathcal{E}(t)e^{-i\omega_0 t}$, with the pulse envelope $\mathcal{E}(t)$ and the central frequency ω_0. The three-level model system, as depicted in Fig. 2(a), consists of the states $|g\rangle$, $|a\rangle$, and $|b\rangle$ with the corresponding transition frequencies $\omega_{ag} = \omega_a - \omega_g$ and $\omega_{ba} = \omega_b - \omega_a$ and nonzero dipole couplings $\mu_{ag} = \langle a|\mu|g\rangle$ and $\mu_{ba} = \langle b|\mu|a\rangle$. Expanding the system state into this basis, i.e., $|\psi(t)\rangle = \sum_{n=g,a,b} c_n(t)|n\rangle$, the laser-atom interaction is described by the TDSE

$$i\hbar \frac{d}{dt} \begin{pmatrix} c_g(t) \\ c_a(t) \\ c_b(t) \end{pmatrix} = \mathcal{H}(t) \begin{pmatrix} c_g(t) \\ c_a(t) \\ c_b(t) \end{pmatrix} \tag{A1}$$

for the population amplitudes $c_n(t)$. The Hamiltonian is given in the dipole approximation by

$$\mathcal{H}(t) = \begin{pmatrix} 0 & -\mu_{ga}E^*(t) & 0 \\ -\mu_{ag}E(t) & \hbar\omega_a & -\mu_{ab}E^*(t) \\ 0 & -\mu_{ba}E(t) & \hbar\omega_b \end{pmatrix}. \tag{A2}$$

The TDSE is solved iteratively on a discrete temporal grid with step size δt using the short-time propagator technique [80–82]

$$\begin{pmatrix} c_g(t + \delta t) \\ c_a(t + \delta t) \\ c_b(t + \delta t) \end{pmatrix} = e^{-i\frac{\delta t}{\hbar}\mathcal{H}(t)} \begin{pmatrix} c_g(t) \\ c_a(t) \\ c_b(t) \end{pmatrix} \tag{A3}$$

and assuming the atom to be initially in the ground state. The photoionization of the population in state $|b\rangle$ is described by the excitation of a final free electron state $|f\rangle$ with $\omega_{fb}(\varepsilon) = \omega_f(\varepsilon) - \omega_b$ as shown in Fig. 2(a).

APPENDIX B: PERTURBATIVE DESCRIPTION OF MPI PHASES

1. Excitation of the state $|a\rangle$

The population amplitude $c_a(t)$ of the state $|a\rangle$ is given by first-order perturbation theory [83,84]

$$c_a(t) = -\frac{\mu_{ag}}{i\hbar} \int_{-\infty}^{t} \mathcal{E}(t') e^{-i\delta_1 t'} dt', \qquad \text{(B1)}$$

with the detuning $\delta_1 = \omega_0 - \omega_{ag}$ and the transition dipole moment μ_{ag}. For $t \to \infty$, Eq. (B1) leads to the well-known result $c_a(\infty) = -\frac{\mu_{ag}}{i\hbar} \tilde{\mathcal{E}}(\delta_1)$. Hence, the final population amplitude of state $|a\rangle$ is given by the spectral amplitude at the transition frequency. In general, by extending the integral in Eq. (B1) up to infinity, utilizing the Heaviside function $\theta(t)$, we obtain

$$c_a(t) = -\frac{\mu_{ag}}{i\hbar} \int_{-\infty}^{\infty} \mathcal{E}(t') e^{-i\delta_1 t'} \theta(t - t') dt'. \qquad \text{(B2)}$$

Applying the Fourier transform in combination with the convolution theorem,[1] the amplitude can be written as

$$c_a(t) = -\frac{\mu_{ag}}{2\pi i\hbar} \left(\left[\pi\delta(\omega) + \frac{ie^{-i\omega t}}{\omega} \right] \otimes \tilde{\mathcal{E}}(\omega) \right)(\delta_1). \qquad \text{(B3)}$$

Note that the convolution integral of the second term is only defined as its Cauchy principal value [85,86], denoted as $\fint$. Hence, the time-dependent population amplitude of $|a\rangle$ reads

$$c_a(t) = -\frac{\mu_{ag}}{2\pi i\hbar} \left(\pi\tilde{\mathcal{E}}(\delta_1) - i\fint_{-\infty}^{\infty} \frac{\tilde{\mathcal{E}}(\omega) e^{i(\omega - \delta_1)t}}{\omega - \delta_1} d\omega \right). \qquad \text{(B4)}$$

a. Resonant excitation of the state $|a\rangle$

For resonant excitation of the state $|a\rangle$, i.e., $\delta_1 = 0$, the population amplitude is given by

$$c_a^{\text{res}}(t) = -\frac{\mu_{ag}}{2\pi i\hbar} \left(\pi\tilde{\mathcal{E}}(0) - i\fint_{-\infty}^{\infty} \frac{\tilde{\mathcal{E}}(\omega) e^{i\omega t}}{\omega} d\omega \right). \qquad \text{(B5)}$$

Since the spectrum $\tilde{\mathcal{E}}(\omega)$ is symmetric, the real part of the integral vanishes and we find

$$c_a^{\text{res}}(t) = -\frac{\mu_{ag}}{2\pi i\hbar} \left(\pi\tilde{\mathcal{E}}(0) + \fint_{-\infty}^{\infty} \frac{\tilde{\mathcal{E}}(\omega) \sin(\omega t)}{\omega} d\omega \right). \qquad \text{(B6)}$$

For $t \to \pm\infty$ the integral is identified with $\pm\pi\tilde{\mathcal{E}}(0)$ by using the definition of the δ distribution [87,88]. Hence, in the resonant case we obtain the known expressions

$$c_a^{\text{res}}(-\infty) = 0 \quad \text{and} \quad c_a^{\text{res}}(\infty) = -\frac{\mu_{ag}}{i\hbar} \tilde{\mathcal{E}}(0). \qquad \text{(B7)}$$

In the following, we consider the nonresonant excitation of the state $|a\rangle$, since the equivalent $4p$ state in the experiment is also excited only near but nonresonantly (see mechanical blocker in Sec. III).

---

[1] Here, we use $\mathcal{F}\{f\}(\omega) := \int_{-\infty}^{\infty} f(t)e^{-i\omega t} dt$ as the convention for the Fourier transform of the function f and the convolution theorem $\mathcal{F}\{fg\}(\omega) = \frac{1}{2\pi}\mathcal{F}\{f\}(\omega) \otimes \mathcal{F}\{g\}(\omega)$.

b. Nonresonant excitation of the state $|a\rangle$

For the nonresonant excitation of $|a\rangle$, i.e., if the detuning δ_1 exceeds the spectral width $\Delta\omega$, it follows $\tilde{\mathcal{E}}(\delta_1) \approx 0$ such that the population amplitude from Eq. (B4) reads

$$c_a^{\text{non}}(t) \approx \frac{\mu_{ag}}{2\pi\hbar} e^{-i\delta_1 t} \fint_{-\infty}^{\infty} \frac{\tilde{\mathcal{E}}(\omega) e^{i\omega t}}{\omega - \delta_1} d\omega. \qquad \text{(B8)}$$

For such a large detuning δ_1 we use a series expansion of the fraction in the integral $\frac{1}{\omega - \delta_1} \approx -\frac{1}{\delta_1} - \frac{\omega}{\delta_1^2} + \mathcal{O}(\frac{\omega^2}{\delta_1^3})$. Thus, the principal value can be approximated by

$$\fint_{-\infty}^{\infty} \frac{\tilde{\mathcal{E}}(\omega) e^{i\omega t}}{\omega - \delta_1} d\omega \approx -2\pi \left(\frac{1}{\delta_1} \mathcal{E}(t) - \frac{i}{\delta_1^2} \frac{\partial\mathcal{E}(t)}{\partial t} \right)$$

$$\approx -\frac{2\pi}{\delta_1} \mathcal{E}(t) e^{-i\zeta t}, \qquad \text{(B9)}$$

with the linear temporal phase $\zeta = \frac{\partial_t^2 \mathcal{E}(0)}{\delta_1 \mathcal{E}(0)}$, neglecting higher-order phases and assuming a symmetric pulse envelope, i.e., $\partial_t \mathcal{E}(0) = 0$. For a Gaussian-shaped envelope the phase ζ takes the form $\zeta = -\frac{\Delta\omega^2}{4\ln(2)\delta_1}$. Therefore the *transient* population amplitude of the state $|a\rangle$ for nonresonant excitation is given by

$$c_a^{\text{non}}(t) \approx -\frac{\mu_{ag}}{\delta_1 \hbar} e^{-i\hat{\delta}_1 t} \mathcal{E}(t), \qquad \text{(B10)}$$

with the reduced detuning $\hat{\delta}_1 = \delta_1 + \zeta$. Hence, for nonresonant excitation the population amplitude $c_a(t)$ of the state $|a\rangle$ follows the temporal field envelope $\mathcal{E}(t)$ and decreases with the detuning via $1/\delta_1$ which also takes into account its sign.

2. Excitation of the state $|b\rangle$

For the excitation of the state $|b\rangle$ via a two-photon process we apply second-order perturbation theory. Assuming a nonresonant excitation of state $|a\rangle$, we build on the results from Sec. B1, i.e., Eq. (B10). The population amplitude of $|b\rangle$ then takes the form

$$c_b(t) = -\frac{\mu_{ba}}{i\hbar} \int_{-\infty}^{t} c_a^{\text{non}}(t') \mathcal{E}(t') e^{-i\omega_0 t'} e^{i\omega_{ba} t'} dt'$$

$$= \frac{\mu_{ba}\mu_{ag}}{i\delta_1\hbar^2} \int_{-\infty}^{t} \mathcal{E}^2(t') e^{-i\delta_2 t'} dt', \qquad \text{(B11)}$$

with $\delta_2 = \hat{\delta}_1 + \omega_0 - \omega_{ba}$. Note that the energy conservation is incorporated by the phase $e^{-i\hat{\delta}_1 t}$ from Eq. (B10), shifting the transition frequency in the second order about the detuning of the nonresonant excitation from first order, i.e., $\omega_{ba} \to \hat{\delta}_1 + \omega_{ba}$. Following an analogous procedure as described in Sec. B1 we find

$$c_b(t) = \frac{\mu_{bg}^{(2)}}{2\pi i\delta_1\hbar^2} \left(\pi\tilde{\mathcal{E}}^{(2)}(\delta_2) - i\fint_{-\infty}^{\infty} \frac{\tilde{\mathcal{E}}^{(2)}(\omega) e^{-i(\delta_2 - \omega)t}}{\omega - \delta_2} d\omega \right), \qquad \text{(B12)}$$

with $\mu_{bg}^{(2)} = \mu_{ba}\mu_{ag}$ as the two-photon transition dipole moment.

a. Resonant excitation of state $|b\rangle$

For two-photon resonant excitation of $|b\rangle$ we assume $\delta_2 = 0$, leading to

$$c_b^{\text{res}}(t) = \frac{\mu_{bg}^{(2)}}{2\pi i \delta_1 \hbar^2} \left(\pi \tilde{\mathcal{E}}^{(2)}(0) - i \fint_{-\infty}^{\infty} \frac{\tilde{\mathcal{E}}^{(2)}(\omega) e^{i\omega t}}{\omega} d\omega \right). \tag{B13}$$

For a symmetric temporal pulse envelope $\mathcal{E}(t)$ and the MPI process to take place in a narrow time window, we can apply a series expansion at $t = 0$. In this way, we find the analytical description for the resonant two-photon probability amplitude:

$$c_b^{\text{res}}(t) = \frac{\mu_{bg}^{(2)}}{2\delta_1 \hbar^2} e^{-i\frac{\pi}{2}} [\tilde{\mathcal{E}}^{(2)}(0) + 2t\mathcal{E}^2(0) + \mathcal{O}(t^3)]. \tag{B14}$$

Note that the term in the order of t^2 vanishes since $\mathcal{E}(t)$ is assumed to exhibit a maximum at $t = 0$. The second term in Eq. (B14) represents the linearly time-increasing population amplitude due to laser excitation and is a sufficient approximation only for $t \approx 0$.

b. Nonresonant excitation of state $|b\rangle$

For nonresonant excitation of the state $|b\rangle$ we use $\delta_2 \neq 0$ in Eq. (B12). Analogous to first-order perturbation theory in Sec. B1b we assume a sufficiently large detuning compared to the spectral width of the second-order spectrum such that $\tilde{\mathcal{E}}^{(2)}(\delta_2) \approx 0$, which leads to

$$c_b^{\text{non}}(t) \approx \frac{\mu_{bg}^{(2)}}{\hbar^2 \delta_1 \delta_2} e^{-i\delta_2 t} \mathcal{E}^2(t). \tag{B15}$$

Due to the large detuning δ_2 in the experiment, we neglect an additional resonance induced quantum phase at this point, i.e., $\delta_2 \approx \hat{\delta}_2$. Similar to Eq. (B10) the population amplitude $c_b^{\text{non}}(t)$ follows the quadratic temporal field envelope and decreases with the detunings via $1/(\delta_1 \delta_2)$ which also takes into account their signs.

3. Excitation of the state $|f\rangle$: Photoionization

To describe the photoionization of the (non-)resonantly excited state $|b\rangle$ into the final free electron state $|f\rangle$ at energy $\varepsilon = \hbar\omega_f - \hbar\omega_{\text{IP}}$, we assume a perturbative one-photon transition with $t \to \infty$. Since we examine both resonant and nonresonant excitation of the state $|b\rangle$ in the experiment (and in Sec. B 2), we distinguish between these two cases also for the photoionization step.

a. Photoionization of the resonantly excited state $|b\rangle$

To describe the photoionization of the resonantly excited state $|b\rangle$, we build on Eq. (B14), which leads to

$$c_f^{\infty,\text{res}}(\varepsilon) \approx \frac{\mu_{fg}^{(3)}}{2\hbar^3 \delta_1} \int_{-\infty}^{\infty} [\tilde{\mathcal{E}}^{(2)}(0) + 2t'\mathcal{E}^2(0)]\mathcal{E}(t') e^{-i\varpi(\varepsilon)t'} dt', \tag{B16}$$

where $\mu_{fg}^{(3)} = \mu_{fb}\mu_{bg}^{(2)}$ denotes the three-photon transition dipole moment and

$$\varpi(\varepsilon) = \omega_0 - \omega_{fb} = \omega_0 - \frac{\varepsilon}{\hbar} + \omega_b - \omega_{\text{IP}} \tag{B17}$$

denotes the photoelectron detuning. Now, the linearly increasing population amplitude in the second term of Eq. (B16) windows the laser electric field of the probe pulse, ensuring the assumption of $t \approx 0$ for the linear approximation in Sec. B2a. This windowing results in a time shift between the probing electric field and the probed photoelectron distribution, resulting in a linear spectral phase [see bottom frame in Fig. 2(c)]. Hence, the second term is equivalent to the first timelike moment of one part of the final population amplitude. Making use of the differentiation theorem for the Fourier transform [87,88] we obtain the photoelectron amplitude

$$c_f^{\infty,\text{res}}(\varepsilon) \approx \frac{\mu_{fg}^{(3)}}{2\hbar^3 \delta_1} \left(\tilde{\mathcal{E}}^{(2)}(0)\tilde{\mathcal{E}}[\varpi(\varepsilon)] - 2i\mathcal{E}^2(0)\frac{\partial\tilde{\mathcal{E}}}{\partial\omega}[\varpi(\varepsilon)] \right). \tag{B18}$$

Around the center contribution of the photoelectron signal at $\varpi(\bar{\varepsilon}) = 0$, the photoelectron amplitude can be approximated by

$$c_f^{\infty,\text{res}}(\varepsilon) \approx \frac{\mu_{fg}^{(3)}}{2\hbar^3 \delta_1} \tilde{\mathcal{E}}^{(2)}(0)\tilde{\mathcal{E}}[\varpi(\varepsilon)] e^{i\xi(\varepsilon)}, \tag{B19}$$

with the additional resonance induced and energy-dependent quantum phase

$$\xi(\varepsilon) = -2\frac{\mathcal{E}^2(0)\frac{\partial\tilde{\mathcal{E}}}{\partial\omega}[\varpi(\varepsilon)]}{\tilde{\mathcal{E}}^{(2)}(0)\tilde{\mathcal{E}}[\varpi(\varepsilon)]}. \tag{B20}$$

Using again a Gaussian-shaped envelope we find

$$\xi(\varepsilon) = 4\sqrt{\frac{\ln(2)}{\pi}}\frac{\varpi(\varepsilon)}{\Delta\omega} = -\frac{\tau_{\text{res}}}{\hbar}\varepsilon + \xi_0, \tag{B21}$$

with the resonance induced time delay $\tau_{\text{res}} = \sqrt{\frac{\ln(2)}{\pi}}\frac{4}{\Delta\omega}$ and an offset $\xi_0 = 4\sqrt{\frac{\ln(2)}{\pi}}\frac{\omega_0 + \omega_b - \omega_{\text{IP}}}{\Delta\omega}$.

b. Photoionization of the nonresonantly excited state $|b\rangle$

Photoionization of the nonresonantly excited state $|b\rangle$ is based on Eq. (B15) and leads to a photoelectron amplitude

$$c_f^{\infty,\text{non}}(\varepsilon) = -\frac{\mu_{fg}^{(3)}}{i\hbar^3 \delta_1 \delta_2} \int_{-\infty}^{\infty} \mathcal{E}^3(t') e^{-i\delta_2 t'} e^{-i\varpi(\varepsilon)t'} dt'$$

$$= i\frac{\mu_{fg}^{(3)}}{\hbar^3 \delta_1 \delta_2} \tilde{\mathcal{E}}^{(3)}[\varpi(\varepsilon) + \delta_2], \tag{B22}$$

which agrees with the results from [83,89] for fully nonresonant MPI processes.

[1] A. Einstein, Über einen die Erzeugung und Verwandlung des Lichtes betreffenden heuristischen Gesichtspunkt, Ann. Phys. (Leipzig) **14**, 165 (1905).

[2] M. Göppert-Mayer, Über Elementarakte mit zwei Quantensprüngen, Ann. Phys. (Leipzig) **401**, 273 (1931).

[3] P. Lambropoulos, Topics on multiphoton processes in atoms, in *Advances in Atomic and Molecular Physics* (Academic Press, Cambridge, 1976), pp. 87–164

[4] F. H. M. Faisal, *Theory of Multiphoton Processes* (Springer, New York, 1987).

[5] Y. Fujimura and S. H. Lin, Multiphoton spectroscopy, in *Encyclopedia of Physical Science and Technology*, 3rd ed., edited by R. A. Meyers (Academic, New York, 2003), pp. 199–229.

[6] V. Letokhov, *Laser Photoionization Spectroscopy* (Elsevier, Amsterdam, 1987).

[7] M. Kitzler and S. Gräfe, *Ultrafast Dynamics Driven by Intense Light Pulses*, Springer Series on Atomic, Optical, and Plasma Physics, Vol. 86 (Springer, New York, 2016).

[8] S. H. Lin, A. A. Villaeys, and Y. Fujimura, *Advances in Multi-Photon Processes and Spectroscopy*, Advances in Multi-Photon Processes and Spectroscopy, Vol. 23 (World Scientific, Singapore, 2016).

[9] D. Bauer, *Computational Strong-Field Quantum Dynamics: Intense Light-Matter Interactions* (De Gruyter, Berlin, 2017), Vol. 1.

[10] P. Hockett, *Quantum Metrology with Photoelectrons: Volume I: Foundations* (Morgan & Claypool, San Rafael, CA, 2018).

[11] K. Yamanouchi, K. Midorikawa, and L. Roso, *Progress in Ultrafast Intense Laser Science XVI* (Springer, New York, 2021).

[12] M. V. Fedorov and A. E. Kazakov, Resonances and saturation in multiphoton bound-free transitions, Prog. Quantum Electron. **13**, 1 (1989).

[13] G. Mainfray and C. Manus, Multiphoton ionization of atoms, Rep. Prog. Phys. **54**, 1333 (1991).

[14] R. Dörner, V. Mergel, O. Jagutzki, L. Spielberger, J. Ullrich, R. Moshammer, and H. Schmidt-Böcking, Cold target recoil ion momentum spectroscopy: A 'momentum microscope' to view atomic collision dynamics, Phys. Rep. **330**, 95 (2000).

[15] M. Wollenhaupt, V. Engel, and T. Baumert, Femtosecond laser photoelectron spectroscopy on atoms and small molecules: Prototype studies in quantum control, Annu. Rev. Phys. Chem. **56**, 25 (2005).

[16] K. L. Reid, Photoelectron angular distributions: Developments in applications to isolated molecular systems, Mol. Phys. **110**, 131 (2012).

[17] E. Goulielmakis, Z. H. Loh, A. Wirth, R. Santra, N. Rohringer, V. S. Yakovlev, S. Zherebtsov, T. Pfeifer, A. M. Azzeer, M. F. Kling, S. R. Leone, and F. Krausz, Real-time observation of valence electron motion, Nature (London) **466**, 739 (2010).

[18] D. M. Villeneuve, P. Hockett, M. J. J. Vrakking, and H. Niikura, Coherent imaging of an attosecond electron wave packet, Science **356**, 1150 (2017).

[19] S. A. Rice and M. Zhao, *Optical Control of Molecular Dynamics* (Wiley, New York, 2000), p. 456.

[20] D. Goswami, Optical pulse shaping approaches to coherent control, Phys. Rep. **374**, 385 (2003).

[21] C. Brif, R. Chakrabarti, and H. Rabitz, Control of quantum phenomena: past, present and future, New J. Phys. **12**, 075008 (2010).

[22] M. Shapiro and P. Brumer, *Quantum Control of Molecular Processes*, 2nd ed. (Wiley, New York, 2012), p. 562.

[23] M. Wollenhaupt, T. Bayer, and T. Baumert, Control of ultrafast electron dynamics with shaped femtosecond laser pulses: From atoms to solids, in *Ultrafast Dynamics Driven by Intense Light Pulses*, edited by S. Gräfe and M. Kitzler (Springer, New York, 2015), Chap. 4, pp. 63–122.

[24] C. Trallero-Herrero, J. L. Cohen, and T. Weinacht, Strong-Field Atomic Phase Matching, Phys. Rev. Lett. **96**, 063603 (2006).

[25] J. M. Ngoko Djiokap, S. X. Hu, L. B. Madsen, N. L. Manakov, A. V. Meremianin, and A. F. Starace, Electron Vortices in Photoionization by Circularly Polarized Attosecond Pulses, Phys. Rev. Lett. **115**, 113004 (2015).

[26] K.-J. Yuan, S. Chelkowski, and A. D. Bandrauk, Photoelectron momentum distributions of molecules in bichromatic circularly polarized attosecond UV laser fields, Phys. Rev. A **93**, 053425 (2016).

[27] D. Pengel, S. Kerbstadt, D. Johannmeyer, L. Englert, T. Bayer, and M. Wollenhaupt, Electron Vortices in Femtosecond Multiphoton Ionization, Phys. Rev. Lett. **118**, 053003 (2017).

[28] S. Kerbstadt, K. Eickhoff, T. Bayer, and M. Wollenhaupt, Odd electron wave packets from cycloidal ultrashort laser fields, Nat. Commun. **10**, 658 (2019).

[29] K. Eickhoff, L. Englert, T. Bayer, and M. Wollenhaupt, Multichromatic polarization-controlled pulse sequences for coherent control of multiphoton ionization, Front. Phys. **9**, 444 (2021).

[30] M. Wollenhaupt, A. Assion, D. Liese, C. Sarpe-Tudoran, T. Baumert, S. Zamith, M. A. Bouchene, B. Girard, A. Flettner, U. Weichmann, and G. Gerber, Interferences of Ultrashort Free Electron Wave Packets, Phys. Rev. Lett. **89**, 173001 (2002).

[31] W. S. Warren, H. Rabitz, and M. Dahleh, Coherent control of quantum dynamics: The dream is alive, Science **259**, 1581 (1993).

[32] H. Rabitz, R. de Vivie-Riedle, M. Motzkus, and K. Kompa, Whither the future of controlling quantum phenomena? Science **288**, 824 (2000).

[33] H. Rabitz, A perspective on controlling quantum phenomena, Faraday Discuss. **153**, 415 (2011).

[34] T. C. Weinacht, J. Ahn, and P. H. Bucksbaum, Controlling the shape of a quantum wavefunction, Nature (London) **397**, 233 (1999).

[35] B. Kaufman, T. Rozgonyi, P. Marquetand, and T. Weinacht, Coherent Control of Internal Conversion in Strong-Field Molecular Ionization, Phys. Rev. Lett. **125**, 053202 (2020).

[36] C. Leichtle, W. P. Schleich, I. S. Averbukh, and M. Shapiro, Quantum State Holography, Phys. Rev. Lett. **80**, 1418 (1998).

[37] I. S. Averbukh, M. Shapiro, C. Leichtle, and W. P. Schleich, Reconstructing wave packets by quantum-state holography, Phys. Rev. A **59**, 2163 (1999).

[38] C. F. de Morisson Faria and A. S. Maxwell, It is all about phases: Ultrafast holographic photoelectron imaging, Rep. Prog. Phys. **83**, 034401 (2020).

[39] M. Isinger, R. J. Squibb, D. Busto, S. Zhong, A. Harth, D. Kroon, S. Nandi, C. L. Arnold, M. Miranda, and J. M. Dahlström, Photoionization in the time and frequency domain, Science **358**, 893 (2017).

[40] M. Swoboda, T. Fordell, K. Klünder, J. M. Dahlström, M. Miranda, C. Buth, K. J. Schafer, J. Mauritsson, A. L'Huillier, and M. Gisselbrecht, Phase Measurement of Resonant

Two-Photon Ionization in Helium, Phys. Rev. Lett. **104**, 103003 (2010).

[41] L. Drescher, T. Witting, O. Kornilov, and M. J. J. Vrakking, Phase dependence of resonant and antiresonant two-photon excitations, Phys. Rev. A **105**, L011101 (2022).

[42] S. Haessler, B. Fabre, J. Higuet, J. Caillat, T. Ruchon, P. Breger, B. Carré, E. Constant, A. Maquet, E. Mével, P. Salières, R. Taïeb, and Y. Mairesse, Phase-resolved attosecond near-threshold photoionization of molecular nitrogen, Phys. Rev. A **80**, 011404(R) (2009).

[43] J. Vos, L. Cattaneo, S. Patchkovskii, T. Zimmermann, C. Cirelli, M. Lucchini, A. Kheifets, A. S. Landsman, and U. Keller, Orientation-dependent stereo Wigner time delay and electron localization in a small molecule, Science **360**, 1326 (2018).

[44] S. Grundmann, D. Trabert, K. Fehre, N. Strenger, A. Pier, L. Kaiser, M. Kircher, M. Weller, S. Eckart, and L. P. H. Schmidt, Zeptosecond birth time delay in molecular photoionization, Science **370**, 339 (2020).

[45] V. Gruson, L. Barreau, A. Jiménez-Galan, F. Risoud, J. Caillat, A. Maquet, B. Carré, F. Lepetit, J. F. Hergott, T. Ruchon, L. Argenti, R. Taïeb, F. Martín, and P. Salières, Attosecond dynamics through a Fano resonance: Monitoring the birth of a photoelectron, Science **354**, 734 (2016).

[46] C. Hofmann, A. S. Landsman, and U. Keller, Attoclock revisited on electron tunnelling time, J. Mod. Opt. **66**, 1052 (2019).

[47] D. Sokolovski and E. Akhmatskaya, No time at the end of the tunnel, Commun. Phys. **1**, 47 (2018).

[48] P. Hockett, E. Frumker, D. M. Villeneuve, and P. B. Corkum, Time delay in molecular photoionization, J. Phys. B **49**, 095602 (2016).

[49] A. Harth, N. Douguet, K. Bartschat, R. Moshammer, and T. Pfeifer, Extracting phase information on continuum-continuum couplings, Phys. Rev. A **99**, 023410 (2019).

[50] J. M. Dahlström, D. Guénot, K. Klünder, M. Gisselbrecht, J. Mauritsson, A. L'Huillier, A. Maquet, and R. Taïeb, Theory of attosecond delays in laser-assisted photoionization, Chem. Phys. **414**, 53 (2013).

[51] M. Schultze, M. Fieá, N. Karpowicz, J. Gagnon, M. Korbman, M. Hofstetter, S. Neppl, A. L. Cavalieri, Y. Komninos, T. Mercouris, C. A. Nocolaides, R. Pazourek, S. Nagele, J. Feist, J. Burgdörfer, A. M. Azzeer, R. Ernstofer, R. Kienberger, U. Kleineberg, E. Goulielmakis *et al.*, Delay in photoemission, Science **328**, 1658 (2010).

[52] J. M. Dahlström, A. L'Huillier, and A. Maquet, Introduction to attosecond delays in photoionization, J. Phys. B **45**, 183001 (2012).

[53] K. Eickhoff, L. Feld, D. Köhnke, T. Bayer, and M. Wollenhaupt, Trichromatic shaper-based quantum state holography, Phys. Rev. A **104**, 052805 (2021).

[54] S. Kerbstadt, D. Pengel, D. Johannmeyer, L. Englert, T. Bayer, and M. Wollenhaupt, Control of photoelectron momentum distributions by bichromatic polarization-shaped laser fields, New J. Phys. **19**, 103017 (2017).

[55] A. Kramida, Y. Rachenko, and J. Reader, NIST atomic spectra database, National Institute of Standards and Technology, Gaithersburg, MD, 2018, The online database is available at https://www.nist.gov/pml/atomic-spectra-database.

[56] M. Wollenhaupt, A. Assion, O. Bazhan, C. Horn, D. Liese, C. Sarpe-Tudoran, M. Winter, and T. Baumert, Control of

interferences in an Autler-Townes doublet: Symmetry of control parameters, Phys. Rev. A **68**, 015401 (2003).

[57] G. A. Garcia, L. Nahon, and I. Powis, Two-dimensional charged particle image inversion using a polar basis function expansion, Rev. Sci. Instrum. **75**, 4989 (2004).

[58] J. C. Diels and W. Rudolph, *Ultrashort Laser Pulse Phenomena* (Academic, New York, 1996).

[59] K. Eickhoff, S. Kerbstadt, T. Bayer, and M. Wollenhaupt, Dynamic quantum state holography, Phys. Rev. A **101**, 013430 (2020).

[60] T. Bayer, M. Wollenhaupt, H. Braun, and T. Baumert, Ultrafast and efficient control of coherent electron dynamics via spods, Adv. Chem. Phys. **159**, 235 (2016).

[61] S. Kerbstadt, L. Englert, T. Bayer, and M. Wollenhaupt, Ultrashort polarization-tailored bichromatic fields, J. Mod. Opt. **64**, 1010 (2017).

[62] S. Kerbstadt, D. Timmer, L. Englert, T. Bayer, and M. Wollenhaupt, Ultrashort polarization-tailored bichromatic fields from a CEP-stable white light supercontinuum, Opt. Express **25**, 12518 (2017).

[63] A. T. J. B. Eppink and D. H. Parker, Velocity map imaging of ions and electrons using electrostatic lenses: Application in photoelectron and photofragment ion imaging of molecular oxygen, Rev. Sci. Instrum. **68**, 3477 (1997).

[64] J. Köhler, M. Wollenhaupt, T. Bayer, C. Sarpe, and T. Baumert, Zeptosecond precision pulse shaping, Opt. Express **19**, 11638 (2011).

[65] A. Wituschek, J. von Vangerow, J. Grzesiak, F. Stienkemeier, and M. Mudrich, A simple photoionization scheme for characterizing electron and ion spectrometers, Rev. Sci. Instrum. **87**, 083105 (2016).

[66] T. Baumert, T. Brixner, V. Seyfried, M. Strehle, and G. Gerber, Femtosecond pulse shaping by an evolutionary algorithm with feedback, Appl. Phys. B **65**, 779 (1997).

[67] D. Yelin, D. Meshulach, and Y. Silberberg, Adaptive femtosecond pulse compression, Opt. Lett. **22**, 1793 (1997).

[68] A. M. Weiner, Femtosecond pulse shaping using spatial light modulators, Rev. Sci. Instrum. **71**, 1929 (2000).

[69] D. Meshulach and Y. Silberberg, Coherent quantum control of two-photon transitions by a femtosecond laser pulse, Nature (London) **396**, 239 (1998).

[70] M. Wollenhaupt, A. Präkelt, C. Sarpe-Tudoran, D. Liese, T. Bayer, and T. Baumert, Femtosecond strong-field quantum control with sinusoidally phase-modulated pulses, Phys. Rev. A **73**, 063409 (2006).

[71] D. Pengel, S. Kerbstadt, L. Englert, T. Bayer, and M. Wollenhaupt, Control of three-dimensional electron vortices from femtosecond multiphoton ionization, Phys. Rev. A **96**, 043426 (2017).

[72] S. Kerbstadt, K. Eickhoff, T. Bayer, and M. Wollenhaupt, Control of free electron wave packets by polarization-tailored ultrashort bichromatic laser fields, Adv. Phys. X **4**, 1672583 (2019).

[73] K. Eickhoff, L. Feld, D. Köhnke, L. Englert, T. Bayer, and M. Wollenhaupt, Coherent control mechanisms in bichromatic multiphoton ionization, J. Phys. B **54**, 164002 (2021).

[74] D. M. Jonas, Two-dimensional femtosecond spectroscopy, Annu. Rev. Phys. Chem. **54**, 425 (2003).

[75] D. Liang, Y. Zhu, and H. Li, Collective Resonance of d States in Rubidium Atoms Probed by Optical Two-Dimensional Coherent Spectroscopy, Phys. Rev. Lett. **128**, 103601 (2022).

[76] P. F. Tekavec, G. A. Lott, and A. H. Marcus, Fluorescence-detected two-dimensional electronic coherence spectroscopy by acousto-optic phase modulation, J. Chem. Phys. **127**, 214307 (2007).

[77] P. F. Tian, D. Keusters, Y. Suzaki, and W. S. Warren, Femtosecond phase-coherent two-dimensional spectroscopy, Science **300**, 1553 (2003).

[78] A. Halpin, P. J. M. Johnson, R. Tempelaar, R. S. Murphy, J. Knoester, T. L. C. Jansen, and R. J. D. Miller, Two-dimensional spectroscopy of a molecular dimer unveils the effects of vibronic coupling on exciton coherences, Nat. Chem. **6**, 196 (2014).

[79] G. Moody and S. T. Cundiff, Advances in multi-dimensional coherent spectroscopy of semiconductor nanostructures, Adv. Phys. X **2**, 641 (2017).

[80] M. D. Feit and J. A. Fleck, Jr., Effect of refraction on spot-size dependence of laser-induced breakdown, Appl. Phys. Lett. **24**, 169 (1974).

[81] C. Cohen-Tannoudji, B. Diu, and F. Laloe, *Quantum Mechanics* (Wiley, New York, 1977), Vol. 1, pp. 3–889.

[82] M. Wollenhaupt, T. Bayer, N. V. Vitanov, and T. Baumert, Three-state selective population of dressed states via generalized spectral phase-step modulation, Phys. Rev. A **81**, 053422 (2010).

[83] D. Meshulach and Y. Silberberg, Coherent quantum control of multiphoton transitions by shaped ultrashort optical pulses, Phys. Rev. A **60**, 1287 (1999).

[84] C. Cohen-Tannoudji, B. Diu, and F. Laloë, *Quantum Mechanics, Volume 3: Fermions, Bosons, Photons, Correlations, and Entanglement* (Wiley, New York, 2019).

[85] N. Dudovich, D. Oron, and Y. Silberberg, Coherent Transient Enhancement of Optically Induced Resonant Transitions, Phys. Rev. Lett. **88**, 123004 (2002).

[86] B. G. Osgood, *Lectures on the Fourier Transform and its Applications*, Vol. 33 (American Mathematical Society, Providence, RI, 2019).

[87] R. Bracewell, *The Fourier Transform and its Applications* (McGraw-Hill, New York, 2000), Vol. 3.

[88] J. W. Goodman, *Introduction to Fourier Optics* (McGraw-Hill, New York, 1996), Vol. 2, pp. xi–441.

[89] N. Dudovich, T. Polack, A. Pe'er, and Y. Silberberg, Simple Route to Strong-Field Coherent Control, Phys. Rev. Lett. **94**, 083002 (2005).